2016-11-15

Sulphide mineral evolution and metal mobility during alteration of the oceanic crust: Insights from ODP Hole 1256D

Patten, C

10.1016/j.gca.2016.08.009
Geochimica et Cosmochimica Acta
Elsevier BV

Sulphide mineral evolution and metal mobility during alteration of the oceanic crust: Insights from ODP Hole 1256D

Patten C.G.C.*[1], Pitcairn I.K.[1], Teagle D.A.H.[2], Harris M.[3]

**Corresponding author: clifford.patten@geo.su.se; +46 (0)8 16 47 37*

[1]Department of Geological Sciences, Stockholm University, Stockholm, Sweden

[2]Ocean and Earth Science, National Oceanography Centre Southampton, University of Southampton, United Kingdom

[3]School of Geography, Earth and Environmental Sciences, Plymouth University, United Kingdom

Abstract

Fluxes of metals during the hydrothermal alteration of the oceanic crust have far reaching effects including buffering of the compositions of the ocean and lithosphere, supporting microbial life and the formation of sulphide ore deposits. The mechanisms responsible for metal mobilisation during the evolution of the oceanic crust are complex and are neither fully constrained nor quantified. Investigations into the mineral reactions that release metals, such as sulphide leaching, would generate better understanding of the controls on metal mobility in the oceanic crust. We investigate the sulphide and oxide mineral paragenesis and the extent to which these minerals control the metal budget in samples from Ocean Drilling Program (ODP) Hole 1256D. The ODP Hole 1256D drill core provides a unique sample suite representative of a complete section of a fast-spreading oceanic crust from the volcanic section down to the plutonic complex. The sulphide population at Hole 1256D is divided into five groups based on mineralogical assemblage, lithological location and texture: the magmatic, metasomatised, high temperature hydrothermal, low temperature and patchy sulphides. The initiation of hydrothermal alteration

by downward flow of moderate temperature (250-350 °C) hydrothermal fluids under oxidising conditions leads to metasomatism of the magmatic sulphides in the sheeted dyke and plutonic complexes. Subsequent increase in the degree of hydrothermal alteration at temperatures >350 ºC under reducing conditions then leads to the leaching of the metasomatised sulphides by rising hydrothermal fluids. Mass balance calculations show that the mobility of Cu, Se and Au occurs through sulphide leaching during high temperature hydrothermal alteration and that the mobility of Zn, As, Sb and Pb is controlled by silicate rather than sulphide alteration. Sulphide leaching is not complete at Hole 1256D and more advanced alteration would mobilise greater masses of metals. Alteration of oxide minerals does not release significant quantities of metal into the hydrothermal fluid at Hole 1256D. Mixing of rising high temperature fluids with low temperature fluids, either in the upper sheeted dyke section or in the transitional zone, triggers local high temperature hydrothermal sulphide precipitation and trapping of Co, Ni, Cu, Zn, As, Ag, Sb, Se, Te, Au, Hg and Pb. In the volcanic section, low temperature fluid circulation (<150 °C) leads to low temperature sulphide precipitation in the form of pyrite fronts that have high As concentrations due to uptake from the circulating fluids. Deep late low temperature circulation in the sheeted dyke and the plutonic complexes results in local precipitation of patchy sulphides and local metal remobilisation. Control of sulphides over Au, Se and Cu throughout fast-spreading mid-oceanic crust history implies that the generation of hydrothermal fluids enriched in these metals, which can eventually form VMS deposits, is strongly controlled by sulphide leaching.

1. Introduction

The cycling of metals in the oceanic crust is an important process which buffers the composition of the lithosphere and oceans, contributes to development of microbial life, and leads to the formation of hydrothermal ore deposits such as volcanogenic massive sulphide (VMS) deposits. Investigations from modern-day oceanic crust (Nesbitt et al., 1987; Alt et al., 1989; Alt, 1995; Alt et al., 1996; Gillis et al., 2001; Bach et al., 2003; Heft et al., 2008; Teagle et al., 2010; Alt et al., 2010; Coogan and Dosso, 2012;

Patten et al., 2015) and ophiolites (e.g. Richardson et al., 1987; Schiffman et al., 1987; Jowitt et al., 2009) suggest that mobilisation of metals from the lower sheeted dyke complex during on-axis high temperature hydrothermal alteration of the oceanic crust is a systematic phenomenon. The high temperature (>350 °C) hydrothermal fluids that leach metals from the lower sheeted dyke section rise buoyantly through upflow zones towards the seafloor where venting occurs (Alt et al., 1989; Alt et al., 2010; Hannington, 2014). During this ascent metals can be lost to mineralised horizons within the upper oceanic crust (Honnorez et al., 1985; Alt et al., 1998; Bach et al., 2003; Alt et al., 2010; Hannington 2013), trapped within VMS deposits (e.g. Fouquet et al., 1988; Herzig and Hannington, 1995; Hannington et al., 1998; Wohlgemuth-Ueberwasser et al., 2015) or vented in hydrothermal plumes and associated sediments (e.g. Feely et al., 1994a; 1994b; Hannington 2013). Mobilisation of metals in the lower sheeted dykes occurs at high temperature and under reduced conditions (>350 °C; e.g. Alt et al., 2010) when solubility of metals is optimal (Seewald and Seyfried; 1990). It is generally assumed that this mobilisation is partly achieved through leaching of magmatic sulphides by hydrothermal fluids (e.g. Keays, 1987; Alt, 1995; Jowitt et al., 2012). The extent, however, to which this mineral reaction controls the release of base metals and other trace metals such as Au, As, Sb, Se and Te into the hydrothermal fluids is neither constrained nor quantified. Reactions involving oxide and silicate minerals have also been shown to mobilise metals including Zn (Doe, 1994; Jowitt et al., 2012). The mineral reactions that produce metal-rich fluids in the modern-day oceanic crust are not well constrained and systematic investigation of the sulphide population evolution during hydrothermal alteration would greatly improve our understanding of metal mobilisation in the oceanic crust.

Located in the Cocos Plate, Pacific Ocean, ODP (Ocean Drilling Program) Hole 1256D is an ideal location to investigate the mobility of metals in a fast-spreading mid-oceanic crust. The 1256D drill core recovers a complete section of the oceanic crust down to the plutonic complex (Wilson et al., 2003; Teagle et al., 2006). The hydrothermal system in the crust at Hole 1256D and the resulting alteration are well defined (Teagle et al., 2006; Alt et al., 2010; Alt and Shanks, 2011; Violay et al., 2013), providing a solid

framework for investigation of mineral reactions leading to metal mobility. Recent investigations on Hole 1256D have shown depletions in whole rock of Cu, Zn and Pb and also of Au, As, and Se concentrations in the deeper parts of the crust (Alt et al., 2010; Patten et al., 2015). These metals are depleted at different crustal levels ranging from the upper sheeted dykes down to the plutonic section implying that multiple mineral reactions may control metal mobility.

This investigation aims to determine the paragenesis and metal contents of the sulphide and oxide minerals in the ODP Hole 1256D crust in order to identify the mineral reactions that release metals into the hydrothermal fluids. We employ in-situ analytical methods including electron-probe microanalysis (EPMA) and laser ablation-inductively coupled plasma mass spectrometer (LA-ICP-MS) analysis to enable quantification of major, minor and trace elements in sulphide and oxide minerals present in the Hole 1256D drill core. We compare our data with published whole-rock concentrations for the same samples from Hole 1256D (Patten et al., 2015) in order to identify the host minerals for this suite of metals and the mineral reactions that liberate metals into hydrothermal fluids during alteration.

2. Geological setting

2.1 ODP Hole 1256D lithologic units

The oceanic crust at drilling site Hole 1256D is a 15 Myr old crust generated from a superfast spreading ridge (~200 mm/yr) and is located in the Cocos Plate (6.736° N, 91.934° W; Wilson et al., 2003). The oceanic crust can be divided into four main lithological units: the volcanic section, the transitional zone, the sheeted dyke complex and the plutonic complex (Fig. 1). The volcanic section is capped by a lava pond on the first 100 m that was formed during off-axis volcanism events (Wilson et al., 2003) underlined by phyric to aphyric sheeted flows, aphyric massive units, pillow lavas and hyaloclastites (Wilson et al., 2003; Teagle et al., 2006). The transitional zone is mainly composed of aphyric sheeted flows with presence of breccias characterised by angular aphyric cryptocrystalline basaltic clasts cemented by

chalcedony, saponite, carbonate, albite, anhydrite and sulphides (Teagle et al., 2006). The sheeted dyke complex comprises massive aphyric basalts with common sub-vertical intrusive contacts (Teagle et al., 2006). Due to intrusion of underlying gabbros, high-temperature recrystallisation occurs in the lower part of the sheeted dyke complex giving a granoblastic texture (Teagle et al., 2006). The plutonic complex is characterised by two gabbro intrusive bodies (Teagle et al., 2006; Koepke et al., 2008). The contacts between the gabbro bodies and the dykes are intrusive, with dyke fragments occurring in the margin of the lower gabbro body (Alt et al., 2010).

2.2 Hydrothermal system and metal mobility

The oceanic hydrothermal system at Hole 1256D can be divided into two simplified domains: an upper low temperature domain and a deeper high temperature domain (Teagle et al., 2006; Alt et al., 2010). The low temperature domain occurs mostly in the volcanic section (250-1004 mbsf) and is characterised by alteration formed from circulation of low-temperature (50°C-185°C) oxidised fluids (Fig. 1, Alt et al., 2010). The associated alteration style is a relatively low-intensity background alteration (2-20 % recrystallisation) where the primary mineralogy is partially replaced with saponite, celadonite, iron oxyhydroxides and chalcedony (Teagle et al., 2006; Alt et al., 2010). Minor pyrite and trace chalcopyrite are associated with this alteration and occur as disseminated grains in the groundmass or in veins. Substantial As enrichment of the volcanic section is associated with this alteration (Patten et al., 2015). Pyrite fronts occur on the borders of oxidised alteration halos (Alt and Shanks, 2011). Significant As and Sb (~20 %) enrichments are associated with these alteration halos (Patten et al., 2015).

The high temperature domain is characterised by alteration formed from circulation of high-temperature (300°C to >650°C; Fig. 1) reduced fluids and occurs in the sheeted dyke and plutonic complexes (1061-1507 mbsf; Alt et al., 2010). The pervasive background alteration is characterised by chlorite, actinolite, albite, titanite and pyrite which correspond to sub-greenschist and greenschist facies conditions (Teagle et al., 2006; Alt et al., 2010). Mobilisation of Au, As and Se associated with the background alteration occurs

in the upper part of the sheeted dyke complex (Patten et al., 2015). Veins of quartz, chlorite, epidote, pyrite, chalcopyrite, magnetite and sphalerite overprint the background alteration and have been interpreted to represent the pathways of rising high temperature fluids from the lower sheeted dyke section and the plutonic complex (Alt et al., 2010). Below 1300 mbsf actinolite is more common than chlorite, indicating an increase in the temperature of alteration (Alt et al., 2010), which also corresponds to an increase in the extent of metal mobilisation in the crust (Cu, Zn, Pb, Au, As and Se; Alt et al., 2010; Patten et al., 2015). The transitional zone and the upper sheeted dyke section correspond to the zone of interaction of the two fluid domains (Fig. 1). The large difference in temperature between the upper and lower fluid domains triggers sulphide mineralisation characterised by a 2.8 m mineralised breccia at 1028 mbsf enriched in Zn, Au, As, Sb, Se and Te (Teagle et al., 2006; Alt et al., 2010; Patten et al., 2015). The sulphide assemblage associated with this mineralisation is pyrite and sphalerite with trace chalcopyrite. A number of similar, but smaller, mineralised veins also occur in the upper sheeted dykes (Teagle et al., 2006; Alt et al., 2010).

3. Sampling and analytical methods

3.1 EPMA analyses

Rock chips from the Hole 1256D drill core were obtained from the collection at the National Oceanographic Centre (NOC) at Southampton, U.K. Optical microscopy by transmitted and reflective light was carried out on 45 polished thin sections representative of the whole crust section. Of the 45 thin polished sections selected, 14 had suitable sulphide and oxide minerals for EPMA and LA-ICP-MS analyses. Electron microprobe analyses were carried out at Uppsala University, Sweden, with a JXA-8530F JEOL SUPERPROBE. For sulphide analyses an accelerating voltage of 20 kV and a beam current of 20 nA were used for a 5μm beam, whereas for oxide analyses an accelerating voltage of 15 kV and a beam current of 10 nA were used. Acquisition time of 20 s and 10 s background was used for sulphide

142 analyses and acquisition time of 10 s and 5 s background was used for oxide analyses. A total of 314 spot
143 analyses were carried out for sulphide minerals on pyrite, chalcopyrite, pyrrhotite, sphalerite, pentlandite,
144 millerite and marcasite (Table 1-5), whilst 180 spot analyses were carried out on oxide minerals on
145 magnetite, titanomagnetite and ilmenite (Table 6). One sigma detection limits for sulphide analyses are 35
146 ppm for S, 43 ppm for Fe, 76 ppm for Cu, 77 ppm for Zn, 65 ppm for Ni and 58 ppm for Co. For oxide
147 minerals detection limits are 104 ppm for Si, 64 ppm for Al, 64 ppm for Mg, 329 ppm for Mn, 161 ppm
148 for Ti, 83 ppm for Ca and 119 ppm for Fe. The Fe_2O_3 content of oxide minerals are calculated using the
149 methods described in Carmichael (1966) and Lepage (2003).

150 3.2 LA-ICP-MS analyses

151 Analyses by LA-ICP-MS were carried out at the PetroTectonics facility at Stockholm University using a
152 NWR-213 nm solid state laser coupled to a ThermoFisher XSeries II quadrupole mass spectrometer. Spot
153 sizes of 30 and 60 μm were used with a laser pulse frequency of 7 Hz and a laser energy density of 8.4
154 $J.cm^{-2}$ for sulphide analyses. A total of 337 spot analyses were carried out on pyrite, chalcopyrite,
155 pyrrhotite, sphalerite and marcasite (Table 1-5). Sulphide grains smaller than 30 μm including pentlandite
156 and millerite could not be efficiently analysed. Each analysis consisted of 60 s background, 40 s ablation
157 and 30 s wash-out. After wash-out, Se isotopes showed long-lived residual signals and additional wash-
158 outs were carried out until the residual signals faded away. Data from EPMA analyses of ^{33}S were used as
159 an internal standard. The following isotopes were monitored: ^{33}S, ^{57}Fe, ^{60}Ni, ^{65}Cu, ^{66}Zn, ^{75}As, ^{76}Se, ^{77}Se,
160 ^{78}Se, ^{82}Se, ^{105}Pd, ^{106}Pd, ^{107}Ag, ^{108}Pd, ^{109}Ag, ^{121}Sb, ^{123}Sb, ^{125}Te, ^{193}Ir, ^{195}Pt, ^{197}Au, ^{200}Hg, ^{202}Hg, ^{208}Pb and the
161 preferred isotopes used for calculations are listed in Appendix A.1. Dwell times were 10 ms/peak for ^{33}S,
162 ^{57}Fe, ^{200}Hg and ^{202}Hg; 20 ms/peak for ^{60}Ni, ^{65}Cu, ^{66}Zn, ^{76}Se, ^{106}Pd, ^{108}Pd and ^{208}Pb; 30 ms/peak for ^{82}Se,
163 ^{105}Pd, ^{107}Ag, ^{109}Ag, ^{125}Te, ^{193}Ir and ^{195}Pt; and 40 ms/peak for ^{121}Sb, ^{123}Sb and ^{197}Au. Calibration was carried
164 out using three reference materials: Trans-1, a synthetic Fe-Ni sulphide doped with 17-25 ppm As, Sb, Se
165 and Te (Wohlgemuth-Ueberwasser et al., 2014); NiS3, a fused nickel sulphide doped with 20-24 ppm Au,
166 Pt, Pd, Ir, Os, Ru and Rh (Gilbert et al., 2013); and MASS-1, a pressed pellet (Fe–Zn–Cu–S) doped with

50–70 ppm As, Ag, Pb, Sb, Se and Te (USGS, Wilson et al., 2002; Appendix A.1). Additionally, MASS-1, NiS3 and PGE_8a were also used as monitors (Appendix A.2). Accuracy and precision of calibrants and monitors are shown in Appendix A.1 and A.2. Isotopes monitored are falling within 10 % of the published values except for ^{121}Sb and ^{197}Au, which are 32 % and 25 % higher respectively than MASS-1. This discrepancy could be due to oxide interferences due to the water present in MASS-1 (Wohlgemuth-Ueberwasser et al., 2014). No appropriate reference materials for monitoring ^{65}Cu, ^{66}Zn, ^{107}Ag, ^{125}Te, ^{200}Hg and ^{208}Pb were available and the implications on the study are detailed in Appendix B. Data reduction and calculation of trace metal concentrations were performed off-line through IOLITE software (Hellstrom et al., 2008, Paton et al., 2011). Detection limits were calculated by IOLITE software at three times the square root of the blanks. Trace metal signals in sulphide minerals are inclusion free which suggests no nugget effect.

Analyses by LA-ICP-MS of oxide minerals were carried out with the same equipment as sulphide analyses. A spot size of 35 μm was used with a laser pulse frequency of 10 Hz. Each analysis consisted of 50 s background, 40 s ablation and 30 s wash-out. Data from EPMA analyses of ^{56}Fe were used for an internal standard. Coarse oxide grains in the plutonic section show fine exsolution textures and their ablation by LA-ICP-MS results in a mixed signal of magnetite and ilmenite. The true Fe concentration is calculated following the Dare et al. (2014) method and using EPMA data for both ilmenite and magnetite. The analyses are thus likely to represent the composition of the oxide before sub-solidus exsolution (Dare et al. 2012). The following isotopes were monitored: ^{23}Na, ^{29}Si, ^{31}P, ^{33}S, ^{44}Ca, ^{47}Ti, ^{49}Ti, ^{51}V, ^{52}Cr, ^{56}Fe, ^{57}Fe, ^{60}Ni, ^{65}Cu, ^{66}Zn, ^{75}As, ^{82}Se, ^{121}Sb, ^{125}Te, ^{195}Pt, ^{197}Au, ^{208}Pb. Dwell times were 2 ms/peak for ^{23}Na, ^{29}Si and ^{44}Ca; 10 ms/peak for ^{51}V, ^{52}Cr, ^{60}Ni, ^{65}Cu, ^{66}Zn and ^{208}Pb; 15 ms/peak for ^{75}As; 20 ms/peak for ^{82}Se and ^{121}Sb; 25 ms/peak for ^{47}Ti, ^{49}Ti and ^{125}Te; 40 ms/peak for ^{33}S; 45 ms/peak for ^{195}Pt; and 60 ms/peak for ^{197}Au. Calibration was performed using NIST 610, a fused glass doped with sixty-one trace elements (Jochum et al., 2011, Appendix A.3). Accuracy and precision of calibration was checked by monitoring the isotopes using BCR-2G a natural basaltic glass (Jochum et al., 2005; Jochum and Nohl, 2008; Jochum

et al., 2014; Appendix A.3). Matrix match standards were not available for oxide analyses and NIST 610 and BCR-2G were used following the methods of (Dare et al., 2012; Nadoll et al., 2014). Good accuracy and precision are reached for ^{47}Ti, ^{49}Ti, ^{51}V, ^{52}Cr, ^{65}Cu, ^{66}Zn, ^{121}Sb and ^{208}Pb (Appendix A.3). Sample analyses for ^{82}Se, ^{125}Te, ^{195}Pt and ^{197}Au are below detection limits. Sulphur was monitored in order to identify possible sulphide inclusions, and Si, Ca and P were monitored to control matrix silicate contamination or titanite alteration of the oxides. Arsenic analyses give signals close to the background with high standard deviation, and furthermore, count per second (CPS) values correlate with Ca suggesting a possible interference of $^{43}Ca^{16}O_2$ on ^{75}As. The ^{75}As data are thus considered to be below the detection limit. The ^{65}Cu values are likely to be a real Cu signal rather than due to $^{49}Ti^{16}O^{+}$ interference, as the oxides with high ^{65}Cu CPS values show no correlation with Ti oxide content. Interference of $^{50}Ti^{16}O^{+}$ on ^{66}Zn is interpreted to be negligible due to the low natural abundance of ^{50}Ti (5.25 %).

4. Results

4.1 Sulphide classification

The sulphide population in Hole 1256D is classified using assemblage, texture, grain size and distribution. Three main processes can account for the majority of sulphide mineral formation: 1) magmatic crystallisation, 2) high temperature fluid circulation, and 3) low temperature fluid circulation.

4.1.1 Magmatic sulphides

Magmatic sulphides consist of pyrrhotite, chalcopyrite and pentlandite that are characteristic of high temperature magmatic sulphides (Fig. 3A and B; Czamanske and Moore, 1977; Mathez, 1979; Peach et al., 1990; Barnes et al. 2006; Patten et al., 2012). They have been observed in two samples from the volcanic section and the plutonic complex at 445 mbsf and 1493 mbsf respectively (Fig. 2) and represent only a minor proportion of the Hole 1256D sulphide population. In the volcanic section, magmatic sulphides occur as 10-50 micron-wide blebs composed of pyrrhotite and chalcopyrite intergrowths

representative of quenched monosulphide solid solution (MSS) and intermediate solid solution (ISS; Fig 3A; e.g. MacLean, 1977; Czamanske and Moore, 1977; Patten et al., 2012). Similar sulphide droplets are observed in fresh MORB glass (Czamanske and Moore, 1977; Mathez, 1979; Francis et al., 1990; Patten et al., 2012) and from other oceanic crust drill core material (MacLean, 1977; Alt et al., 1989). In the plutonic complex magmatic sulphides do not have systematic shape but are larger than in the volcanic section (up to hundreds of microns in width), and are composed of pyrrhotite, chalcopyrite and pentlandite (Fig. 3B). The latter occurs as a lamellae exsolution within the pyrrhotite, which is characteristic of slowly cooled magmatic sulphides that have exsolved from MSS and ISS (Fig. 3B; Kelly and Vaughan, 1983; Alt and Anderson, 1991; Barnes et al., 2006; Dare et al., 2010; Djon et al., 2012). Mineral proportions by visual estimation are 90 % pyrrhotite with trace exsolution pentlandite and 10 % chalcopyrite.

Quenched sulphide blebs from the volcanic section are a mixture of MSS and ISS and have different composition from the magmatic sulphides in the plutonic complex (Table 1). The sulphide blebs from the volcanic section have the Fe and S composition of pyrrhotite but show high and variable Cu, Zn, Pb and trace metals concentrations due to contamination from small chalcopyrite inclusions (Table 1). Large pyrrhotite grains from the plutonic complex contain trace amounts of Co, Ni, Cu, Zn, As, Se, Ag, Te, Au and Pb. Concentrations of Sb, platinum group elements (PGE; Pt, Pd, Ir, Os, Ru and Rh) and Hg are below detection limits. Chalcopyrite from the plutonic complex has higher concentrations of Zn (1169 ppm, 2-5000 ppm), Ag (5.38 ± 3.38), Te (2.82 ± 1.36 ppm), and Pb (3.29 ppm, 0.28-10.6 ppm) than pyrrhotite and pentlandite, and contains trace amounts of Co, Ni, Se and Au (Table 1). Concentrations of As, Sb, PGEs and Hg are below detection limit in chalcopyrite. Selenium and Au concentrations in pyrrhotite and chalcopyrite are similar (45.2 ± 8.2 ppm and 49.6 ± 18.7 ppm for Se respectively, and 0.023 ± 0.019 ppm and 0.027 ± 0.017 for Au respectively, Table 1). Pentlandite, unlike pyrrhotite and chalcopyrite, does not show stoichiometric composition due to high concentrations of Co (16.5 ± 3.6 wt.%; Table 1) that can substitute for Fe (19.8 ± 6.4 wt.%) and Ni (21.5 ± 4.0 wt.%; Riley, 1977). The pentlandite Cu and Zn

239 contents are below the detection limit for EPMA and analyses by LA-ICP-MS were impossible due to too
240 small grain size.

241 *4.1.2 Metasomatised sulphides*

242 Metasomatised sulphides consist of pyrite, chalcopyrite, millerite and magnetite, an assemblage that is
243 characteristic of recrystallised magmatic sulphides (Fig. 3C, D, E and F; Table 2; Alt., 1989). This group
244 occurs mostly in the sheeted dyke and the plutonic complexes with a few occurrences in the volcanic
245 section (Fig. 2). Pyrite is the most abundant mineral of the group and occurs as grains up to hundreds of
246 microns in size that are commonly anhedral in shape and can be porous in places (Fig. 3D). Chalcopyrite
247 is homogeneous and occurs either as grains associated with the pyrite or as isolated grains. It ranges in
248 size from a few microns up to tens of microns. Millerite generally occurs at the contact between pyrite and
249 chalcopyrite and is the smallest phase of the assemblage with a size that does not exceed a few microns
250 (Fig. 3F). Magnetite occurs as small micron-sized grains associated with pyrite, often forming rims
251 surrounding the sulphide assemblage (Fig. 3C, D and E).

252 Metasomatised pyrites contain traces of Co, Ni, Cu, Zn, As, Sb, Te, Hg, Au and Pb (Table 2). Few grains
253 show signals above the detection limit for Pd and Pt, and other PGEs are below detection limits. Trace
254 metal concentrations in metasomatised pyrites are highly variable and positively skewed as highlighted by
255 the discrepancy between the average and median values (Table 2). This discrepancy is due to localised
256 enrichment of trace metals during metasomatism and leaching (see discussion). Selenium and As can
257 substitute for S in pyrite (e.g. Genna and Gaboury, 2015) and the Se/As ratio is a useful parameter to
258 determine pyrite genesis in magmatic or hydrothermal systems (Duran et al., 2015). Metasomatised
259 pyrites are characterised by high Se/As, suggesting a magmatic origin (Duran et al., 2015), and
260 intermediate to high Ni content (Fig. 4). Chalcopyrite contains traces of Co, Ni, As, Se, Ag, Sb, Te, Hg,
261 Au and Pb (Table 2) whereas PGEs are below detection limit. Trace metal concentrations in
262 metasomatised chalcopyrite are also variable but not as pronounced as in the metasomatised pyrites (Table

2). Millerite has low Ni (51.3 ± 12.3 wt.%) relative to stoichiometric value, which can be accounted for by the high concentration of Co and Fe (4 ± 1.9 wt.% and 6.4 ± 7.6 wt.%, respectively).

4.1.3 High temperature hydrothermal sulphides

High temperature hydrothermal sulphides represent the largest sulphide occurrence of the Hole 1256D. They occur mostly in the upper sheeted dyke section and the transitional zone (Fig. 2) within mineralised breccias, quartz-chlorite dominated veins or as disseminated grains (Fig. 1). They are characterised by euhedral to subhedral grains of pyrite, chalcopyrite and sphalerite. Pyrite grains vary in size from small (tens of microns) grains that form porous aggregates, to large (hundreds of microns) grains (Fig. 5A, B and C). Chalcopyrite is common in the upper sheeted dyke section but scarce in the transitional zone (Fig. 2). Conversely, sphalerite occurs in trace amounts in veins from the upper sheeted dyke section but is the second most common sulphide mineral in the transitional zone mineralised breccias (Fig. 2). In the upper sheeted dyke section sphalerite commonly shows the chalcopyrite disease texture (Fig. 5A) whereas in the transitional zone it is euhedral to subhedral (Fig. 5C). This distribution of sulphide phases is similar to that reported in the mineralised zone in Hole 504B (Honnorez et al., 1985), although the sulphide mineralisation in Hole 1256D is less well developed than in Hole 504B.

High temperature pyrites contain trace amounts of Co, Ni, Cu, Zn, As, Sb, Te, Hg, Au and Pb (Table 3). Few grains show signals above the detection limit for Pd and other PGEs are below detection limit. Relative to metasomatised pyrites, high temperature pyrites have higher median values of As (23.7 ppm), Ag (2.39 ppm) and Au (0.12 ppm) but lower Ni (30.0 ppm), Cu (25.9 ppm) and Pb (14.6 ppm); other trace metals are within the same order of magnitude (Table 2 and 3). The variability in trace metal concentrations in high temperature pyrites is most likely due to different trapping efficiency during sulphide precipitation. Differences in composition between high temperatures pyrite from the transitional zone and the upper sheeted dyke section can be observed (Table 3). The former shows higher As (31.1 ± 18.7 ppm), Sb (0.67 ppm, 0.04-4.07 ppm), Au (0.12 ± 0.10 ppm) and Pb (104.6 ppm, 0.5-408 ppm) where the latter shows higher Ni (236 ppm, 11.8-1225 ppm). Other trace metals are within the same order of

magnitude in the two different groups. High temperature pyrites are overall characterised by low Ni concentration and large Se/As (Fig. 4). Chalcopyrites contain trace amounts of Ni, Zn, As, Pd, Sb, Te, Au and Pb whereas Co, PGE and Hg are below detection limit (Table 3). Zinc concentrations in sphalerite are low (55.2 ± 2.8 wt.%) due to variable concentration of Fe (8.5 ± 3.1 wt.%). The Fe/Zn ratio of inclusion-free sphalerite can be used to calculate the minimum fluid temperature from which sphalerite precipitates (Keith et al., 2014). An average temperature of 378 ± 24 °C is calculated for sphalerite from the transitional zone from EPMA data. Calculation for sphalerite from the upper sheeted dyke section cannot be carried out because of systematic chalcopyrite disease texture (Keith et al., 2014). This texture also explains the high Cu variability in sphalerite (up to 3.8 wt.%; Table 3) especially in the upper sheeted dyke section. Sphalerite contain trace amounts of Co, Ni, Cu, Zn, As, Se, Ag, Sb, Hg and Pb. Within the high temperature hydrothermal sulphides, pyrites have the highest Co, As, Te and Au concentrations, whereas Ni, Se and Ag concentrations are higher in chalcopyrite, and Sb, Hg and Pb in sphalerite (Table 3; e.g. Monecke et al., 2016).

4.1.4 Low temperature sulphides

Sulphides from the low temperature sulphide group are common throughout the volcanic section and are characterised by pyrite, millerite and trace chalcopyrite (Fig. 2). Micron sized pyrite and chalcopyrite grains are commonly disseminated in the ground mass associated with the background alteration, but the bulk of the low temperature sulphide occurs as “pyrite fronts” composed of pyrite and marcasite (Andrews, 1979). They occur as narrow zones hundreds of microns wide and centimeters long in which they replace the silicate matrix and fill pores and cracks (Figs. 5D, E and F). These pyrite fronts occur on the border of alteration halos (Wilson et al., 2003; Alt. and Shanks, 2011) or oxidation zones (Andrews, 1979).

Distinction between pyrite and marcasite grains during in-situ analyses was not possible and the data in Table 4 represents average content of both minerals. They contain trace amounts of Co, Ni, Cu, Zn, As, Se, Ag, Sb and Pb (Table 4). Tellurium, PGEs, Au and Hg are below detection limits. Low temperature

pyrites show the highest As concentrations of the different sulphide groups (99 ± 66 ppm) but have low Cu (9.6 ppm, 1.01-57 ppm), Zn (3.3 ± 2.8 ppm), Ag (0.20 ± 0.10 ppm) and Pb (1.37 ± 1.26 ppm) relative to metasomatised and high temperature pyrites (Table 4). Because of high As concentrations, low temperature pyrites show low As/Se and are also characterized by high Ni content (Figure 4). Rare chalcopyrite grains were too small for in-situ analysis.

4.1.5 Patchy sulphides

Patchy sulphides occur in the lower volcanic section, transitional zone, sheeted dyke and plutonic complexes (Fig. 2). They are characterised by a spherical web-like network up to one centimetre wide that replaces the silicate matrix (Fig 5H and I). Silicate phenocrysts, oxides and other sulphides are also affected. The patches do not seem to be associated with any specific type of silicate alteration. Pyrite is the most common mineral and is generally homogeneous and anhedral, but can also be porous. Minor chalcopyrite also occurs and one sample from the plutonic complex contains patches of marcasite.

Metal concentrations in the patchy sulphides (Table 5) are similar to the low temperature sulphides and are low relative to metasomatised and high temperature sulphides (Table 1-5). Pyrites contain trace amounts of Co, Ni, Cu, Zn, As, Se, Ag, Sb, Te, Au and Pb (Table 5). Platinum group elements and Hg are below detection limits. Similarly pyrite fronts, patchy pyrites are characterised by low Se/As and high Ni content (Fig. 4) which suggest similar pargenesis. A few in-situ analyses of chalcopyrite show trace amounts of Co, Ni, Zn, Ag and Pb (Table 5).

4.2 Oxide classification

Oxide minerals are common in Hole 1256D and are classified into three main groups based on their texture, size, lithological occurrence and mineralogical assemblage: skeletal magmatic titanomagnetite, coarse magmatic magnetite-ilmenite and hydrothermal-related magnetite. Skeletal titanomagnetites are the most common oxide mineral and occur in the volcanic section and the sheeted dyke complex. They are present as micrometric disseminated skeletal grains or as dendritic chains (tens of microns, Fig. 6A;

337 Wilson et al., 2003). Their presence in the ground mass is ubiquitous (Wilson et al., 2003) and is generally
338 confined to interstitial areas (Fig. 6A; Kempton et al., 1985). Disseminated micrometric ilmenite and
339 magnetite grains are also locally observed. Titanomagnetites have TiO_2 > 2 wt.%, average 17.8 ± 6.5 wt.%
340 TiO_2 and have the highest V, Cu, Zn, Sb and Pb concentrations of the three oxide groups (Table 6).

341 The second group of oxide minerals in Hole 1256D are magmatic related coarse grained magnetite and
342 ilmenite (few mm) occurring in the plutonic complex (e.g. oxide gabbro; Teagle et al., 2006). They are
343 characterised by coarse magnetite with trellis patterns of ilmenite exsolution or by ilmenite with magnetite
344 exsolution (Fig. 6B; e.g. Kent et al., 1978). Homogeneous grains of magnetite or ilmenite are also present.
345 Ilmenites average 49.7 ± 6.9 wt.% TiO_2 and magnetites average of 3.4 ± 1.4 wt.% TiO_2 (Table 6). Trace
346 element concentrations analysed by LA-ICP-MS are a mixed signal of both magnetite and ilmenite and are
347 listed in Table 6. Coarse magnetite-ilmenites have the highest Cr and the lowest Cu content of the three
348 oxide group (Table 6).

349 The third group corresponds to secondary magnetite grains that are associated with hydrothermal fluid
350 circulation. They either occur as precipitated euhedral grains within veins, as disseminated subhedral
351 grains or as replacement of primary silicate and sulphide phases (Fig. 6C an D). They are present mostly
352 in the sheeted dyke complex. Hydrothermal magnetites have low TiO_2 concentrations (1.7 ± 1.5 wt.%) and
353 are characterised by the highest Ni content and the lowest V, Zn and Pb content (Table 6). The magnetite
354 rims associated with the metasomatised sulphide are part of the hydrothermal oxide group but, given their
355 small size, only two grains were large enough to be analysed by LA-ICP-MS, with one of the two showing
356 considerable sulphide contamination.

357 5. Discussion

358 The sulphide classification described above indicates that sulphides are sensitive to the different styles of
359 hydrothermal alteration in the oceanic crust. In-situ analyses reveal significant variations in trace metal

content between the different sulphide mineral groups. The comparison between trace element concentrations in the different sulphide groups with whole rock metal concentrations allows some assessment of the degree to which the sulphide minerals control the trace metal budget in these rocks. This mass balance indicates which mineral reactions are responsible for metal mobilisation during the hydrothermal alteration of the oceanic crust.

5.1 The magmatic assemblage

Some primary sulphides and oxides have been sufficiently shielded from later hydrothermal fluid circulation that their magmatic characteristics have been preserved. Magmatic sulphides are, however, scarce in the Hole 1256D due to the extensive hydrothermal alteration. Magmatic S concentrations in Hole 1256D average 1250 ± 200 ppm (Alt and Shanks, 2011), which is high enough for a MOR basaltic melt to be sulphide-saturated before eruption (e.g. Mathez, 1979; Li and Ripley, 2005). Magmatic sulphides observed in Hole 1256D were most likely present as sulphide liquid within the magma prior to crystallisation, similar to the sulphide droplets observed in fresh MORB glass (Mathez, 1976; Peach et al., 1990; Patten et al., 2013). These sulphide droplets are quenched from ~1200 ºC to seawater temperature in a few minutes (Moore, 1975), resulting in their crystallisation as MSS and ISS intergrowths characteristic of magmatic temperatures (1200-1000 ºC, Fig. 3A and 7; e.g. Czamanske and Moore, 1977; Mathez, 1979; Patten et al., 2012). Magmatic sulphide droplets in the volcanic section are considered to represent these high-temperature sulphide assemblages. In the plutonic complex, however, where sulphide liquid is preserved from quenching, the observation of pyrrhotite with pentlandite exsolution as lamellae implies that the sulphides cooled below 650 ºC, enabling the MSS and the ISS to exsolve to the observed phases (Fig. 3A and 7; Kelly and Vaughan, 1983; Patten et al., 2012).

The composition of magmatic sulphides from Hole 1256D (Table 1) differs slightly from previous reports of fresh MORB sulphide droplets through having lower chalcophile element concentrations (Co, Ni, Cu, Se, Ag, Te, Au; e.g. Patten et al., 2013). Differences in concentrations are attributed to different primary

384 magmatic composition rather than effect of alteration. Arsenic can be used as an indicator for fluid
385 interaction with sulphides as it is a highly mobile element in fluids (e.g. Smedley and Kinniburgh, 2002).
386 Pyrrhotite grains from the plutonic section have low As concentration (0.95 ± 0.11 ppm, Table 1)
387 suggesting limited interaction with circulating fluids whereas sulphide blebs in the volcanic section have
388 relatively high As concentration (5.12 ± 1.34 ppm) suggesting possible contamination by low temperature
389 fluids. The magmatic sulphides from the plutonic complex can be interpreted to have conserved their true
390 primary magmatic composition most likely due to limited interaction with hydrothermal fluids as
391 implicated by the low water-rock ratio (<1) below 1300 mbsf (Gao et al., 2012).

392 In the volcanic section, disseminated titanomagnetites have skeletal texture characteristic of a magmatic
393 origin and occur in interstitial areas suggesting late-stage crystallisation (Kempton et al., 1985). Trellis
394 pattern of ilmenite-magnetite exsolutions in coarse grain oxides in the plutonic complex represent sub-
395 solidus oxy-exsolution during magma cooling (Dare et al., 2012), also indicating its magmatic origin. The
396 trace element composition of the skeletal titanomagnetite composition indicates temperatures around
397 ~500°C (Fig. 8D). Magmatic oxide minerals host minor Cu and Zn, traces of Pb and Sb and no As, Se, Te
398 or Au. This elemental distribution can be partly explained by the Goldschmidt rule for cation substitution
399 within the oxide structure, with Cu^{2+} and Zn^{2+} being substituted with Fe^{2+} in the octahedral sites, whereas
400 other metallic cations cannot be substituted with Fe cations (e.g. Dare et al., 2012, Nadoll et al., 2014).
401 Skeletal titanomagnetites are richer in Cu, Zn, Sb and Pb than the coarse magnetite-ilmenites (Table 6).
402 Samples hosting skeletal titanomagnetites from the volcanic section are slightly more evolved than those
403 hosting coarse magnetite-ilmenites from the plutonic section (Fig. 1). The primary metal content of the
404 magma, however, is unlikely to account for the different metal contents of the two oxide groups as Cu, Zn,
405 Pb and Sb show variable behaviour during magmatic differentiation with Cu for example, being enriched
406 in more primitive melts and Pb, Zn and Sb being enriched in more evolved melts (Jenner et al., 2012). A
407 more likely alternative is that the metal content of the magmatic oxides is related to the cooling rate of the
408 magma and the presence of sulphide with which competition for metal trapping occurs (Dare et al., 2014).

In the volcanic rocks hosting skeletal titanomagnetite, the quick cooling rate of the magma at eruption may have inhibited effective diffusion of metals to the sulphide blebs (low R-factor; Barnes and Lightfoot, 2005) allowing metals to be partly incorporated into oxides, with the converse occurring in the plutonic rocks that host coarse magnetite-ilmenite and coarse magmatic sulphides.

5.2 Effects of hydrothermal fluid circulation in the lower oceanic crust

5.2.1 Sulphide metasomatism

Hydrothermal fluid circulation in the lower portion of the oceanic crust leads to sub-solidus recrystallisation of the magmatic sulphides into metasomatised sulphides (Alt et al., 1989). The pyrrhotite, chalcopyrite and pentlandite are recrystallised to secondary pyrite, chalcopyrite, millerite and magnetite. Two processes can trigger the recrystallisation of pyrrhotite to secondary metasomatised pyrite: reduction of seawater sulphate at high temperature (>250 ºC) or oxidation of the magmatic sulphides. Seawater sulphate (SO_4^{2-}) reduction in the oceanic crust provides S as sulphide to the rock, leading to pyrrhotite (FeS) recrystallisation to secondary pyrite (FeS_2; Shanks and Seyfried; 1987):

$$7FeS + 8H^+ + SO_4^{2-} = 4FeS_2 + 4H_2O + 3Fe^+ \quad [1]$$

The isotopic sulphur signature of metasomatised pyrite suggests that this reaction occurs in the sheeted dyke complex at Hole 504B (Alt et al., 1989). Alternatively, oxidation of pyrrhotite and pentlandite ($Fe_4Ni_5S_8$) can lead to the formation of pyrite, magnetite (Fe_3O_4) and millerite (NiS) at moderate temperature (up to 350 ºC, Craig and Kullerud, 1969; Craig, 1973; Barnes et al., 2009; Djon et al., 2012):

$$FeS + Fe_4Ni_5S_8 + 2O_2 = 2FeS_2 + Fe_3O_4 + 5NiS \quad [2]$$

The textures of the metasomatised sulphides in Hole 1256D support the latter process as they are characterised by metasomatised pyrite surrounded by a magnetite rim which represents an oxidation front where fluids have reacted with the pyrrhotite (Fig. 3C, D and E). Formation of metasomatised pyrite by

sulphate reduction is also likely to occur in Hole 1256D but the almost ubiquitous presence of magnetite associated with metasomatised sulphides suggests that the oxidation is the dominant reaction. Trace element concentrations of the magnetite rims suggest oxidation reaction at temperatures ~300 ºC (Fig. 8B; Nadoll et al., 2014). These temperatures and the mineralogical assemblage of metasomatised sulphides suggest that metasomatism is most likely driven by deep influx of recharging hydrothermal fluids at moderate temperature (200-350 ºC; Alt et al., 1986; Alt and Chaussidon, 1989; Coumou et al. 2008; Harris 2015) into the lower part of Hole 1256D during on-axis hydrothermal alteration (Tolstoy et al., 2008; Coumou et al., 2008). These fluids penetrate into the sheeted dyke complex along dyke margins (Harris et al., 2015) most probably during the early stages of hydrothermal alteration (Alt et al., 2010; Harris et al., 2015).

5.2.2 Sulphide leaching

During on-axis hydrothermal fluid circulation, equilibration of the "recharging" moderate temperature hydrothermal fluids with the surrounding rocks in the sheeted dyke and plutonic complexes increases their temperature (>350ºC) and acidity, and causes reduction of the fluids (e.g. Alt et al., 1986; Alt et al., 2010). These buoyant, acidic and reduced high-temperature hydrothermal fluids eventually rise within the sheeted dyke and plutonic complexes towards the seafloor following the similar pathways to those taken by the recharging fluids (Alt et al., 2010; Harris et al., 2015). Under these conditions, metal solubility in hydrothermal fluids significantly increases (Seewald and Seyfreid, 1990) and sulphide minerals undergo leaching and dissolution (Fig. 7). These conditions correlate with the onset of depletion of metals from the Hole 1256D whole rock samples (Alt et al., 2010; Patten et al., 2015), The local preservation of magmatic and metasomatised sulphides in Hole 1256D indicates, however, that sulphide leaching is not complete (Fig. 2 and 9). Leaching of sulphides is likely to be dependent upon the degree of interaction with the high temperature fluids on a grain-scale as highlighted by the preservation of variably leached sulphide grains within the same sample. Degrees of leaching range from full preservation of pristine magmatic and metasomatised sulphides (Fig. 3E), to extensively leached sulphides (Fig. 9). In the extensively leached

sulphides, chalcopyrite grains are more abundant than pyrite (Fig. 9A, C and D) which suggests that chalcopyrite is less reactive to high temperature fluid circulation than pyrite (Fig. 10). This is supported by experimental studies that show Cu is less soluble than other base metals in hydrothermal fluids at temperature >300 °C in reduced conditions (e.g. Hemley et al., 1992). Pyrite occurs either as porous patches or isolated grains within the magnetite rim, and these textures indicate a significant sulphide volume loss (Fig. 9B, C and D). This volume loss is due to progressive release of S and Fe to the high temperature fluids (Crerar et al., 1978):

$$FeS_{2_s} + 2H^+_{aq} + H_2O_{aq} = Fe^{2+}_{aq} + 2H_2S_{aq} + \frac{1}{2}O_{2_{aq}} \quad [3]$$

Behaviour of trace metals during sulphide leaching is dependent on their solubilities in the high temperature fluids, which are controlled by temperature, pressure, pH, fO_2, fS_2 and fluid composition (e.g. Cl^-; Crerar et al., 1978; Hannington and Scott, 1989; Seewald and Seyfried, 1990; Hemley et al., 1992; Gibert et al., 1998).

5.2.3 Trace metal behaviour during metasomatism and leaching

Major and trace metal concentrations vary considerably during metasomatism and leaching of the magmatic sulphides (Table 1 and 2). Using median values, metasomatised pyrite shows higher concentrations of Co (+7 %), Cu (+ 2528%), Zn (+334 %), As (+265 %), Se (+91 %), Ag (+469 %), Te (+89 %), Au (+115 %) and Pb (+1466 %) relative to pyrrhotite (Table 1 and 2). Only Ni shows lower concentrations (-21 %; Table 1 and 2). Although the moderate temperature hydrothermal fluids that drive sulphide metasomatism probably contain some trace metals, is it highly unlikely that they systematically enrich the metasomatised sulphides in trace metals to such extents. Increases in trace metal concentrations in metasomatised sulphides are most likely due to residual enrichment during successive sulphide volume loss and local metal diffusion between mineral grains. During metasomatism, diffusion of Fe from pyrrhotite forms the magnetite rim (Equation 2). This process leads to sulphide volume loss and recrystallisation of pyrrhotite to pyrite with a corresponding S increase of +34.3 % and Fe decrease of -21.4 % of the sulphide assemblage (Table 1 and 2, Fig. 10). The residual metal enrichment caused by the

conversion of pyrrhotite to pyrite, however, only partially explains the large enrichments of trace metals observed in metasomatised pyrite. Additional concentration of trace metals occurs during leaching where preferential mobilisation of Fe and S into the hydrothermal fluids leads to further sulphide loss (equation [3]). The behaviour of Se clearly highlights this two-step process as demonstrated by the variation in the S/Se ratio during metasomatism and leaching (Fig. 11A). During metasomatism the S/Se is constant as S and Se are equally concentrated during Fe diffusion to magnetite, but as leaching occurs the S/Se decreases as S is preferentially mobilised by the hydrothermal fluids along with Fe (Fig. 11A). The high concentrations of Co, Zn, Ag, Se, Te and Au in pyrite are most likely explained by the combined effects of metasomatism and leaching (Fig. 11). Although Sb is below detection limit in pyrrhotite the range of concentrations in metasomatised pyrites suggest similar behaviour (Table 2). The extreme concentration increases of Cu (+ 2528%) and Pb (+1466 %), and the decrease in Ni concentrations (-21 %) in metasomatised pyrites cannot be explained solely by sulphide volume loss and we suggest that diffusion of these elements between the different sulphide phases present in the assemblage occurs. Nickel is likely to diffuse into the millerite from both pyrrhotite and pentlandite (Table 1 and 2; Fig. 10) whereas Cu is likely to diffuse from the chalcopyrite to the pyrite during metasomatism, and Pb from surrounding silicates (Table 1 and 2; Fig. 10). Changes in the trace metal distribution between magmatic and metasomatised sulphides suggests that localised grain-scale metal mobility occurs during metasomatisation (Fig 10), but bulk mobilisation of metals from the rock does not occur until the onset of sulphide leaching. Ultimately, if sulphide leaching goes to completion then all trace elements hosted in metasomatised sulphides will be mobilised into the high temperature fluids (Fig. 10).

5.2.4 Oxide alteration by hydrothermal fluid circulation

Although oxide minerals show some evidence of alteration they are less affected by high temperature fluid circulation than sulphide minerals. Laverne et al. (2006) report breakdown of titanomagnetite to hydroschlormite during low temperature alteration. Additionally Alt et al. (2010) reports increasing titanomagnetite alteration below 660 mbsf. The Si+Ca/Ti ratio increases with depth indicating greater

alteration (Fig. 8B). No systematic variation of metal concentrations with the Si+Ca/Ti ratio can be observed in oxides indicating that, the contrary to sulphides, alteration of these minerals in Hole 1256D does not release metals (Fig. 8E, F, G and H).

5.3 Mineral precipitation during high temperature fluid circulation

In the upper sheeted dyke and transitional zone, on-axis mixing of ascending high temperature fluids with the low temperature fluids prevailing in the volcanic section triggers significant sulphide precipitation forming a 2.8 m mineralised breccia at 1028 mbsf (Teagle et al., 2006; Alt et al., 2010; Fig. 7). Fluid inclusion microthermometry suggests that fluid mixing and sulphide precipitation occurred at temperatures between 320 °C and 450 °C (Alt et al., 2010) and at high fluid-rock ratios (Harris et al., 2015). Such temperatures are consistent with the minimum hydrothermal fluid temperature of 378 ± 24 °C estimated from Fe/Zn in sphalerite (Keith et al., 2014). The mineralogical assemblages and trace metal concentrations in pyrite vary between the transitional zone and the upper sheeted dykes suggesting different mineralisation in these two areas. Temperature controlled metal zonation is common in VMS deposits: precipitation of chalcopyrite and Ni-bearing pyrite occur at higher temperatures than sphalerite and As, Sb, Au and Pb-bearing pyrite (Hannington and Scott, 1989; Metz and Trefry, 2000; Genna and Gaboury, 2015; Keith et al., 2016; Monecke et al., 2016) and a similar zonation is observed in Hole 1256D between the upper sheeted dyke section and the transitional zone (Table 3). The Se/As ratio tends to be lower in pyrites from the transitional zone relative to those in the upper sheeted dyke section (Fig. 4) which can be attributed to an increased input of low temperature fluids leading to temperature decrease (Genna and Gaboury, 2015), with possible As contamination from these fluids. The low Ni content and variable Se/As ratios of hydrothermal pyrites are distinctly different from metasomatised pyrites highlighting the different origin between the two sulphide groups. Although high temperature hydrothermal sulphides have significant trace metal concentrations (Table 3) their impact on the bulk fluxes of metals from the lower sheeted dykes is minimal (Nesbitt et al., 1987; Patten et al,. 2015). Hydrothermal magnetites are also interpreted to be generated from the circulation of high temperature

fluids. Their composition, characterised by low Ti content (Fig. 8C), and texture confirm their hydrothermal origin and suggests that they formed at similar temperatures (~300-500 °C) to the high temperature sulphides (Fig. 8D).

5.4 Sulphide formation during low temperature fluid circulation

In the volcanic section pyrite fronts locally occur on the margins of significantly oxidised zones referred to as alteration halos (e.g. Andrews, 1979; Alt and Shanks, 2001; Fig. 7). Andrews (1979) proposes that the pyrite fronts form from leaching of magmatic sulfides from the alteration halos by low temperature fluids. The presence of marcasite indicates acidic solution (<5 pH) and partly oxidised soluble species such as thiosulphate (Murowchick and Barnes, 1986). Alt and Shanks (2011), however, argue that there is insufficient sulfide in the alteration halos to account for that in the pyrite fronts, and additional S is required from microbial seawater sulfate reduction. The formation of alteration halos and pyrite fronts occurs at the latest stages of fluid circulation during off-axis low temperature alteration (Alt et al., 2010; Harris et al., 2015) at higher water-rock ratio than the background alteration (Teagle et al., 2006; Gao et al., 2012). Significant As enrichment occurs in the alteration halos and the pyrite fronts occurs (Patten et al, 2015) causing the low Se/As ratio due to As input from the low temperature fluids (Fig. 4). In sulphide-free samples, which also show As enrichment (Patten et al., 2015), As is likely to be hosted in Fe-oxyhydroxide minerals (Wolthers et al., 1998; Smedley and Kinniburgh, 2002; Han et al., 2012). High Ni concentrations in pyrite fronts (Table 4; Fig. 4) can be explained by Ni incorporation in pyrite at low temperature and under anoxic conditions (Morse and Luther, 1999). Along with As, significant whole-rock enrichment of Sb occurs in the volcanic section (Patten et al., 2015), but this enrichment is associated with secondary silicates rather than the low temperature sulphides (Fig. 12; Jochum and Verna, 1996).

In the sheeted dyke and plutonic complexes the patchy sulphides share numerous characteristics with low temperature sulphides although they are not associated with any specific alteration. They have similar mineralogical assemblages of pyrite, minor marcasite and trace chalcopyrite (Fig. 2), and replacement

textures (Fig. 5). Pyrites from the patchy sulphide group are characterised by low Se/As ratio and high Ni and falls within the field of the low temperature pyrite (Fig. 4). These similarities between the two sulphide groups suggest similar paragenesis, implying that the patchy sulphide group formed during late-stage off axis low temperature fluid circulation in the sheeted dyke and plutonic complexes. Patchy sulphides have moderate trace metal concentrations (Table 5), suggesting metal remobilisation from the surrounding rocks during off axis fluid circulation.

5.5 Mass balance

A mass balance calculation has been carried out to investigate the degree to which sulphide minerals control the whole-rock metal concentrations in Hole 1256D samples. The mass balance has been carried out only on samples containing one dominant sulphide group. Hypothetical whole rock compositions were calculated for each sample assuming that all the metals present in the sample are solely hosted by sulphides. The total mass of sulfide is calculated using whole rock S concentration (Patten et al., 2015). The total mass of sulfide and the compositions of the different phases in the sulphide group are then used to calculate the hypothetical whole rock compositions, which are then compared to the real whole rock compositions to give the % of each metal that is hosted as sulphide (Appendix B). Several significant errors are associated with the mass balance calculation, such as the problem of comparing observations from a 2D thin section surface with analyses of a 3D sample volume, and error propagations are discussed in Appendix B. Because of these errors, the mass balance is considered to be semi-quantitative but the results still enable evaluation of the extent to which the sulphides control the whole rock metals budget in Hole 1256D. The results are classified into >50 %, 10-50 % and <10 % sulphide hosting.

Although based on a low number of samples (n=2), the mass balance for samples hosting magmatic sulphides suggests that Cu, Se, Te and Au are strongly controlled (>50 %) by sulphides (Fig. 12) whereas Zn, As, Sb and Pb are mostly controlled by silicate and oxide minerals (sulphide <10 %, Fig. 12; Gurney and Ahrens, 1973; Doe et al., 1994; Alt, 1995). Similarly to magmatic sulphides, metasomatised sulphides

581 strongly control Cu, Se, Te and Au (>50 %), partly control As and Pb (10-50 %) and weakly control Zn
582 and Sb (<10 %; Fig. 12). The similarity in mass balance between the two sulphide groups suggests that
583 during metasomatism, metals undergo local grain-scale diffusion but are not extensively mobilised by the
584 moderate temperature hydrothermal fluids (250-350 °C; Fig. 10). Samples hosting high temperature
585 sulphides, located in the upper sheeted dykes and the transitional zone, are the only ones where sulphides
586 control most of the whole rock metal budget (Fig. 12). In these samples pyrite hosts most of the Se, Te,
587 Au and Pb whereas Cu is controlled by chalcopyrite and Zn by sphalerite (Fig. 12). Arsenic and Sb are
588 only partly controlled by sulphides in these samples. In the volcanic section, mass balance calculations of
589 samples hosting low temperature sulphides suggest that Cu and As are strongly controlled and Se partly
590 controlled by sulphides, whereas Zn, Sb and Pb are poorly controlled by sulphides (Fig. 12). Finally, the
591 mass balance calculation of the patchy sulphide group suggests that only Cu is strongly hosted by these
592 sulphides, whereas As, Se, Sb, Te and Au are partly controlled and Zn and Pb are poorly controlled by
593 sulphides (Fig. 12).

594 5.6 Mineralogical controls on metal mobilisation

595 In the oceanic crust, significant mobilisation of metals occurs from the lower sheeted dyke section during
596 high temperature hydrothermal fluid circulation (e.g. Hole 504B: Alt et al., 1996; Nesbitt et al., 1987;
597 Bach et al., 2003; Hole 1256D: Teagle et al., 2006; Alt et al., 2010; Patten et al., 2015; Pito deep: Heft et
598 al., 2008). In Hole 1256D, Au, As, Se, Cu, Zn and Pb are variably depleted relative to primary crustal
599 compositions (-46 %, -27 %, -27 %, -10 %, -8 % and -44 % respectively; Patten et al., 2015). As
600 magmatic and metasomatised sulphides have strong control over Cu, Se and Au budgets (Fig. 12) at the
601 time of high temperature hydrothermal alteration, sulphide leaching is clearly a key mineral reaction for
602 mobilisation of these metals. This is strongly supported by the large whole-rock metal depletions in
603 samples hosting metasomatised and leached sulphide minerals (i.e in samples below 1061 mbsf; Fig. 13).
604 Additionally, variability in whole rock metal depletions can be partly explained by the variable behaviour
605 of the metals during sulphide leaching. Copper, Se and Au are strongly hosted by magmatic and

606 metasomatised sulphides but Cu shows lower whole rock depletions (-10 %) than Se and Au (-27 % and -
607 46 % respectively) in the sheeted dyke and plutonic complexes. Selenium and Au are principally hosted in
608 pyrite (Fig. 12) which is reactive to sulphide leaching (Fig. 9) explaining the higher whole rock depletions,
609 whereas Cu is hosted in chalcopyrite (Fig. 12) which is more resistant to leaching (Fig. 9A, B and 10). The
610 depletions of As, Zn and Pb in Hole 1256D (-27 %, -8% and -44 % respectively) are neither associated
611 with sulphide leaching (Fig. 12) or oxide alteration (Fig. 8F) but most likely with alteration of silicate
612 minerals (Doe et al., 1994). Oxide minerals host significant Zn and some Sb (Table 6; Doe et al., 1994;
613 Gurney and Ahrens, 1973) and increased alteration of these minerals could lead to greater depletion of
614 these metals. Antimony and Te show no significant whole rock variation in Hole 1256D during high
615 temperature hydrothermal alteration (Patten et al., 2015) and more intensive alteration would be required
616 to mobilise these elements (Fig. 12).

617 The different metal behaviour during sulphide leaching, as summarised in Figure 10, and the control of
618 oxide and silicate mineral alteration on mobility of some elements indicates that peak mobilisation for
619 each metal occurs at different stages, and under different conditions. Trace metals hosted in pyrite are
620 likely to be released during initiation of leaching, whereas Cu and trace metals in chalcopyrite would be
621 released at higher temperature during sulphide leaching leading to significant fractionation of metals in the
622 hydrothermal fluid. This process may affect the relative metal contents of the high temperature
623 hydrothermal fluids through time.

624 5.7 Metal-rich hydrothermal fluids and formation of VMS deposits

625 At ODP Hole 1256D, the masses of metals mobilised during thigh temperature hydrothermal alteration of
626 the sheeted dyke and plutonic complexes is sufficient to form modern-day low tonnage mafic type VMS
627 deposits (Patten et al., 2015) such as those found at the EPR 13 °N (Fouquet et al., 1988) or the TAG
628 VMS deposit (e.g. Hannington et al., 1998). Different reactions provide different metals to the fluids with
629 sulphide leaching providing the Cu, Se and Au, and silicate reactions providing the As, Sb, Zn and Pb

630 (Figs. 12 and 13). Lack of known VMS deposits in the vicinity of Hole 1256D, however, highlights the
631 importance of metal trapping mechanisms for formation of VMS deposits. The preservation of both
632 magmatic and metasomatised (i.e. not fully leached) sulphides in Hole 1256D crust implies that sulphide
633 leaching has not gone to completion. The preservation of these sulphides in Hole 1256D is most likely due
634 to the relative low water-rock ratio in the lower part of Hole 1256D (w/r <1; Gao et al., 2012) which may
635 be a feature of fast-spreading ridge oceanic crust compared to other tectonic settings such as ophiolites
636 which are more extensively altered (Alt and Teagle; 2000). More extensive hydrothermal alteration would
637 lead to total sulphide leaching and an increase in the quantity of metal mobilised from the oceanic crust.
638 Epidosite zones observed in ophiolitic systems and interpreted as the source areas for metals enriched in
639 associated VMS deposits (Jowitt et al., 2012) are likely to represent this advanced stage of sulphide
640 leaching.

641 # 6. Conclusions

642 In-situ analyses of the sulphide and oxide minerals present in the ODP Hole 1256D drill core enables
643 determination of their paragenesis during the evolution of the oceanic crust and evaluation of the extent to
644 which extend they control bulk metal behaviour in the crust (Fig. 7). The main outcomes of this study are:

645 • Five main groups of sulphides occur in ODP Hole 1256D: magmatic, metasomatised, high
646 temperature, low temperature and patchy sulphides. Three groups of oxides occur: magmatic skeletal
647 titanomagnetite, magmatic coarse magnetite-ilmenite and hydrothermal related magnetite.
648 • Initiation of hydrothermal fluid circulation in the lower sheeted dyke section and the plutonic
649 complex at moderate temperature (~300 ºC) and relatively oxidising conditions leads to
650 metasomatism of the magmatic sulphides. Recrystallisation of pyrrhotite, chalcopyrite and
651 pentlandite to form secondary pyrite, chalcopyrite, millerite and magnetite drives significant diffusion
652 of metals between the sulphide phases and the surrounding silicates and oxides, although little bulk
653 metal mobilisation to the circulating hydrothermal fluids occurs at this stage.

- Increase in hydrothermal alteration temperature (>350 ºC) under reduced conditions leads to progressive leaching and dissolution of the metasomatised sulphides. Semi-quantitative mass balance calculations suggest that sulphide leaching is responsible for the release of most Cu, Se and Au during the hydrothermal alteration of the lower sheeted dyke section and the plutonic complex. The different behaviour of trace metals during sulphide leaching suggests that they have different timing for peak mobilisation. Chalcopyrite is less reactive to leaching than pyrite implying that Cu and the metals hosted in chalcopyrite are released during the highest temperature alteration conditions. The mobilisation of As, Zn and Pb is controlled by silicate reactions rather than sulfide leaching.
- A fraction of the metal mobilised by the high temperature hydrothermal fluids are trapped within mineralised veins and breccias as high temperature sulphides in the upper sheeted dyke section and the transitional zone during mixing with low temperature fluids. The high temperature pyrite, sphalerite and chalcopyrite have high and variable trace metal concentrations which highlight different behaviour during sulphide precipitation and metal trapping.
- Late off-axis circulation of low temperature fluids (<150 °C) in the oceanic crust leads to the local formation of pyrite fronts in the volcanic section and to patchy sulphides in the sheeted dyke and plutonic complexes. High As enrichments in the pyrite fronts suggests significant uptake from the circulating low temperature fluids in the volcanic section whereas the moderate trace metal concentrations in the patchy sulphides suggests late metal remobilisation within the sheeted dyke and plutonic complexes.
- The hydrothermal fluids that form during alteration of the lower sheeted dyke units in Hole 1256D are sufficiently metal-rich to form low tonnage VMS deposits on the seafloor. The metal enrichments in the fluids are driven by different mineral reactions with Cu, Se and Au mobilised by sulfide leaching, and As, Zn and Pb mobilised by silicate reactions. An increase in alteration would likely lead to total sulphide leaching and metal release leading to higher metal budget of the hydrothermal fluids increasing the likeliness of VMS deposits formation.

7. Acknowledgements

This work was funded by Stockholm University and by the Swedish Research Council (PRG 621-2007-4539). The authors would like to thank Cora Wohlgemuth-Ueberwasser and Jarek Majka for in-situ analyses. Analyses by EPMA were funded by the 2013 ECORD research grant. This research used samples provided by the ODP and IODP. The ODP was sponsored by the National Foundation (NSF) and participating countries under management of Joint Oceanographic Institutions (JOI). The IODP was supported by NSF; Japan's Ministry of Education, Culture, Sports, Science, and Technology; the European Consortium for Ocean Research Drilling; the Australia-New Zealand IODP Consortium; and the People's Republic of China Ministry of Science and Technology.

8. References

Alt J. C. (1995) Subseafloor processes in mid-ocean ridge hydrothermal systems. *Seafloor Hydrothermal Systems: Physical, Chemical, Biological, and Geological Interactions*, 85-114.

Alt J. C., Honnorez J., Laverne C. and Emmermann R. (1986) Hydrothermal alteration of a 1 km section through the upper oceanic crust, Deep Sea Drilling Project Hole 504B: Mineralogy, chemistry and evolution of seawater basalt interactions. *J. Geophys. Res. Solid Earth* **91**, 10309-10335.

Alt J. C., Anderson T. F. and Bonnell L. (1989) The geochemistry of sulfur in a 1.3 km section of hydrothermally altered oceanic crust, DSDP Hole 504B. *Geochim. Cosmochim. Acta* **53**, 1011-1023.

Alt J. C. and Chaussidon M. (1989) Ion microprobe analyses of the sulfur isotopic composition of sulfides in hydrothermally altered rocks, DSDP/ODP Hole 504B1. *Proceedings of the Ocean Drilling Programme, Scientific Results* **111**, 41-45.

699 Alt J. C. and Anderson T. F. (1991) The mineralogy and isotopic composition of sulfur in Layer 3 gabbros
700 from the Indian Ocean, OOP Hole 735B. *Proceedings of the Ocean Drilling Programme, Scientific*
701 *Results* **118**, 113-125.

702 Alt J. C., Laverne C., Vanko D. A., Tartarotti P., Teagle D. A., Bach W., Zuleger E., Erzinger J.,
703 Honnorez I. and Pezard P. A. (1996) Hydrothermal alteration of a section of upper oceanic crust in the
704 eastern equatorial Pacific: A synthesis of results from Site 504 (DSDP Legs 69, 70, and 83, and ODP Legs
705 111, 137, 140, and 148). *Proceedings of the Ocean Drilling Programme, Scientific Results* **148**, 417-434.

706 Alt J. C., Teagle D. A. H., Brewer T., Shanks W. C. and Halliday A. (1998) Alteration and mineralization
707 of an oceanic forearc and the ophiolite-ocean crust analogy. *J. Geophys. Res. Solid Earth* **103**, 12365-
708 12380.

709 Alt J. C. and Teagle D. A. (2000) Hydrothermal alteration and fluid fluxes in ophiolites and oceanic crust.
710 *Sp. Pa. Geol. Soc. Am.*, 273-282.

711 Alt J. C, Laverne C., Coggon R. M., Teagle D. A. H., Banerjee N. R., Morgan S., Smith-Duque C. E.,
712 Harris M. and Galli L. (2010) Subsurface structure of a submarine hydrothermal system in ocean crust
713 formed at the East Pacific Rise, ODP/IODP Site 1256. *Geochem. Geophys. Geosyst.* **11**.

714 Alt J. C. and Shanks W. C. (2011) Microbial sulfate reduction and the sulfur budget for a complete section
715 of altered oceanic basalts, IODP Hole 1256D (eastern Pacific). *Earth Planet. Sci. Lett.* **310**,73-83.

716 Andrews A. J. (1979) On the effect of low-temperature seawater-basalt interaction on the distribution of
717 sulfur in oceanic crust, layer 2. *Earth Planet. Sci. Lett.* **46**, 68-80.

718 Bach W., Peucker-Ehrenbrink B., Hart S. R. and Blusztajn J. S. (2003) Geochemistry of hydrothermally
719 altered oceanic crust: DSDP/ODP Hole 504B–Implications for seawater-crust exchange budgets and Sr-
720 and Pb-isotopic evolution of the mantle *Geochem. Geophys. Geosyst.* **4**.

721 Barnes S. J. and Lightfoot P. C. (2005) Formation of magmatic nickel-sulfide ore deposits and processses
722 affecting their copper and platinum-group element contents. *Econ. Geol. 100th Anniv. Vol.*, 179-213.

723 Barnes S. J., Cox R. A. and Zientek M. L. (2006) Platinum-group element, gold, silver and base metal
724 distribution in compositionally zoned sulfide droplets from the Medvezky Creek Mine, Noril'sk, Russia.
725 *Contrib. Miner. Pet.* **152**, 187-200.

726 Barnes S. J., Wells M. A. and Verrall M. R. (2009) Effects of magmatic processes, serpentinization, and
727 talc-carbonate alteration on sulfide mineralogy and ore textures in the Black Swan disseminated nickel
728 sulfide deposit, Yilgarn Craton. *Econ. Geol.* **104**, 539-562.

729 Carmichael I. S. (1966) The iron-titanium oxides of salic volcanic rocks and their associated
730 ferromagnesian silicates. *Contr. Min. and Pet.* **14**, 36-64.

731 Coogan L. A. and Dosso S. (2012) An internally consistent, probabilistic, determination of ridge-axis
732 hydrothermal fluxes from basalt-hosted systems. *Earth Planet. Sci. Lett.* **323**, 92-101.

733 Coumou, D., Driesner, T. and Heinrich, C. (2008) The structure and dynamics of mid-ocean ridge
734 hydrothermal systems. *Sci.* **321**, 1825-1828.

735 Craig J., Kullerud G. (1969) Phase relations in the Cu-Fe-Ni-S system and their application to magmatic
736 ore deposits. *Econ. Geol. Monogr.* **4**, 344-358.

737 Craig J. R. (1973) Pyrite-pentlandite assemblages and other low temperature relations in the Fe-Ni-S
738 system. *Am. J. Sci.* **273**, 496-510.

739 Crerar D. A., Susak N., Borcsik M. and Schwartz S. (1978) Solubility of the buffer assemblage pyrite+
740 pyrrhotite+ magnetite in NaCl solutions from 200 to 350 C. *Geochim. Cosmochim. Acta* **42**, 1427-1437.

741 Czamanske G. K., Moore J. G. (1977) Composition and phase chemistry of sulfide globules in basalt from
742 the Mid-Atlantic Ridge rift valley near 37°N lat. *Geol. Soc. Am. Bul.* **88**, 587-599.

743 Dare S., Barnes S.-J. and Prichard H. (2010) The distribution of platinum group elements (PGE) and other
744 chalcophile elements among sulfides from the Creighton Ni–Cu–PGE sulfide deposit, Sudbury, Canada,
745 and the origin of palladium in pentlandite. *Min Dep* **45**, 765-793.

746 Dare S. A., Barnes S.-J. and Beaudoin G. (2012) Variation in trace element content of magnetite
747 crystallized from a fractionating sulfide liquid, Sudbury, Canada: Implications for provenance
748 discrimination. *Geochim. Cosmochim. Acta* **88**, 27-50.

749 Dare S. A., Barnes S.-J., Beaudoin G., Méric J., Boutroy E. and Potvin-Doucet C. (2014) Trace elements
750 in magnetite as petrogenetic indicators. *Min Dep* **49**, 785-796.

751 Djon M. and Barnes S.-J. Changes in sulfides and platinum-group minerals with the degree of alteration in
752 the Roby, Twilight, and High Grade Zones of the Lac des Iles Complex, Ontario, Canada. *Min Dep* **47**, 1-
753 22.

754 Doe B. R. (1994) Zinc, copper, and lead in mid-ocean ridge basalts and the source rock control on Zn/Pb
755 in ocean-ridge hydrothermal deposits. *Geochim. Cosmochim. Acta* **58**, 2215-2223.

756 Duran C., Barnes S.-J. and Corkery J. (2015) Chalcophile and platinum-group element distribution in
757 pyrites from the sulfide-rich pods of the Lac des Iles Pd deposits, Western Ontario, Canada: Implications
758 for post-cumulus re-equilibration of the ore and the use of pyrite compositions in exploration. *J. Geochem.*
759 *Expl*. **158**, 223-242.

760 Feely R., Gendron J., Baker E. and Lebon G. (1994a) Hydrothermal plumes along the East Pacific Rise, 8
761 40′ to 11 50′ N: Particle distribution and composition. *Earth Planet. Sci. Lett.***128**, 19-36.

762 Feely R. A., Massoth G. J., Trefry J. H., Baker E. T., Paulson A. J. and Lebon G. T. (1994b) Composition
763 and sedimentation of hydrothermal plume particles from North Cleft segment, Juan de Fuca Ridge. *J.*
764 *Geophys. Res. Solid Earth* **99**, 4985-5006.

765 Fouquet Y., Auclair G., Cambon P. and Etoubleau J. (1988) Geological setting and mineralogical and
766 geochemical investigations on sulfide deposits near 13 N on the East Pacific Rise. *Marine Geol.* **84**, 145-
767 178.

768 Francis R. D. (1990) Sulfide globules in mid-ocean ridge basalts (MORB), and the effect of oxygen
769 abundance in Fe-S-O liquids on the ability of those liquids to partition metals from MORB and komatiite
770 magmas. *Chem. Geol.* **85**, 199-213.

771 Gao Y., Vils F., Cooper K., Banerjee N., Harris M., Hoefs J., Teagle D., Casey J., Elliott T. and Laverne
772 C. (2012) Downhole variation of lithium and oxygen isotopic compositions of oceanic crust at East Pacific
773 Rise, ODP Site 1256. *Geochem. Geophys. Geosyst.* **13**.

774 Genna D. and Gaboury D. (2015) Deciphering the Hydrothermal Evolution of a VMS System by LA-ICP-
775 MS Using Trace Elements in Pyrite: An Example from the Bracemac-McLeod Deposits, Abitibi, Canada,
776 and Implications for Exploration. *Econ. Geol.* **110**, 2087-2108.

777 Gibert F., Pascal M.-L. and Pichavant M. (1998) Gold solubility and speciation in hydrothermal solutions:
778 Experimental study of the stability of hydrosulphide complex of gold (AuHS) at 350 to 450 C and 500
779 bars. *Geochim. Cosmochim. Acta* **62**, 2931-2947.

780 Gilbert S., Danyushevsky L., Robinson P., Wohlgemuth-Ueberwasser C., Pearson N., Savard D., Norman
781 M. and Hanley J. (2013) A comparative study of five reference materials and the lombard meteorite for
782 the determination of the Platinum-Group Elements and Gold by LA-ICP-MS. *Geostat. Geoanal. Res.* **37**,
783 51-64.

784 Gillis K. M., Muehlenbachs K., Stewart M., Gleeson T. and Karson J. (2001) Fluid flow patterns in fast
785 spreading East Pacific Rise crust exposed at Hess Deep. *J. Geophys. Res. Solid Earth* **106**, 26311-26329.

786 Godel B. (2013) High-resolution X-ray computed tomography and its application to ore deposits: From
787 data acquisition to quantitative three-dimensional measurements with case studies from Ni-Cu-PGE
788 deposits. *Econ. Geol.* **108**, 2005-2019.

789 Gurney J. and Ahrens L. (1973) The zinc content of some ultramafic and basic rocks. *Trans. Geol. Soc.*
790 *So. Afr.* **73**, 301-307.

791 Han D. S., Batchelor B. and Abdel-Wahab A. (2012) Sorption of selenium (IV) and selenium (VI) onto
792 synthetic pyrite (FeS 2): Spectroscopic and microscopic analyses. *J. Col Inter. Sci.* **368**, 496-504.

793 Hannington M. D. (2013) The role of black smokers in the Cu mass balance of the oceanic crust. *Earth*
794 *Planet. Sci. Lett.* **374**, 215-226.

795 Hannington M. D. (2014) 13.18 - Volcanogenic Massive Sulfide Deposits. *Holland, Heinrich D, in:*
796 *Turekian, K.K. (Ed.), Treatise on Geochemistry (Second Edition). Elsevier, Oxford,* 463-488.

797 Hannington M. D. and Scott S. D. (1989) Sulfidation equilibria as guides to gold mineralization in
798 volcanogenic massive sulfides; evidence from sulfide mineralogy and the composition of sphalerite. *Econ.*
799 *Geol.* **84**, 1978-1995.

800 Hannington M. D., Galley A. G., Herzig P. M. and Petersen S. (1998) 28. Comparison of the TAG mound
801 and stockwork complex with Cyprus-type massive sulfide deposits. *Proceedings of the Ocean Drilling*
802 *Program: Scientific Results*, 389.

803 Harris M., Coggon R. M., Smith-Duque C. E., Cooper M. J., Milton J. A. and Teagle D. A. H. (2015)
804 Channelling of hydrothermal fluids during the accretion and evolution of the upper oceanic crust: Sr
805 isotope evidence from ODP Hole 1256D. *Earth Planet. Sci. Lett.* **416**, 56-66.

806 Heft K. L., Gillis K. M., Pollock M. A., Karson J. A. and Klein E. M. (2008) Role of upwelling
807 hydrothermal fluids in the development of alteration patterns at fast spreading ridges: Evidence from the
808 sheeted dike complex at Pito Deep. *Geochem. Geophys. Geosyst.* **9**.

809 Hellstrom J., Paton C., Woodhead J. and Hergt J. (2008) Iolite: software for spatially resolved LA-(quad
810 and MC) ICPMS analysis. *Mineral. Ass. Can. Short Course Series* **40**, 343-348.

811 Helmy H. M., Ballhaus C., Wohlgemuth-Ueberwasser C., Fonseca R. O. C. and Laurenz V. (2010)
812 Partitioning of Se, As, Sb, Te and Bi between monosulfide solid solution and sulfide melt – Application to
813 magmatic sulfide deposits. *Geochim. Cosmochim. Acta* **74**, 6174-6179.

814 Hemley J., Cygan G., Fein J., Robinson G. and d'Angelo W. (1992) Hydrothermal ore-forming processes
815 in the light of studies in rock-buffered systems; I, Iron-copper-zinc-lead sulfide solubility relations. *Econ.*
816 *Geol.* **87**, 1-22.

817 Herzig P. M. and Hannington M. D. (1995) Polymetallic massive sulfides at the modern seafloor A
818 review. *Ore Geol. Rev.* **10**, 95-115.

819 Honnorez J. A., Jeffrey C.; Honnorez-Guerstein, B. M.; Laverne, C.; Muehlenbachs, K.; Saltzman, E.
820 (1985) Stockwork-like sulfide mineralization in young oceanic crust; Deep Sea Drilling Project Hole
821 504B. *Initial Reports of the Deep Sea Drilling Project* **83**, 263-282.

822 Jenner F. E. and O'Neill H. S. (2012) Analysis of 60 elements in 616 ocean floor basaltic glasses.
823 *Geochem. Geophys. Geosyst.* **13**.

824 Ji-Hai Y., Xiu-Chun Z., Chen-Zi F., Ling-Hao Z., Dong-Yang S., Ze-Rong J., Ming-Yue H. and Li-Jun K.
825 (2012) Quantitative analysis of sulfide minerals by laser ablation-inductively coupled plasma-mass
826 spectrometry using glass reference materials with matrix normalization plus sulfur internal standardization
827 calibration. *Chin. J. of Anal. Chem.* **40**, 201-207.

828 Jowitt S. M., Jenkin G. R. T., Coogan L. A. and Naden J. (2012) Quantifying the release of base metals
829 from source rocks for volcanogenic massive sulfide deposits: Effects of protolith composition and
830 alteration mineralogy. *J. Geochem. Expl.* **118**, 47-59.

831 Jochum K. and Verma S. (1996) Extreme enrichment of Sb, Tl and other trace elements in altered MORB.
832 *Chem. Geol.* **130**, 289-299.

833 Jochum K. P., Willbold M., Raczek I., Stoll B. and Herwig K. (2005) Chemical characterisation of the
834 USGS reference glasses GSA-1G, GSC-1G, GSD-1G, GSE-1G, BCR-2G, BHVO-2G and BIR-1G Using
835 EPMA, ID-TIMS, ID-ICP-MS and LA-ICP-MS. *Geostat. Geoanal. Res.* **29**, 285-302.

836 Jochum K. P., Weis U., Stoll B., Kuzmin D., Yang Q., Raczek I., Jacob D. E., Stracke A., Birbaum K. and
837 Frick D. A. (2011) Determination of reference values for NIST SRM 610–617 glasses following ISO
838 guidelines. *Geostat. Geoanal. Res.* **35**, 397-429.

839 Jochum K. P. and Nohl U. (2008) Reference materials in geochemistry and environmental research and
840 the GeoReM database. *Chem. Geol.* **253**, 50-53.

841 Jochum K. P., Stoll B., Weis U., Jacob D. E., Mertz-Kraus R. and Andreae M. O. (2014) Non-Matrix-
842 Matched Calibration for the Multi-Element Analysis of Geological and Environmental Samples Using 200
843 nm Femtosecond LA-ICP-MS: A Comparison with Nanosecond Lasers. *Geostat. Geoanal. Res.* **38**, 265-
844 292.

845 Keays R. R. (1987) Principles of mobilization (dissolution) of metals in mafic and ultramafic rocks—the
846 role of immiscible magmatic sulphides in the generation of hydrothermal gold and volcanogenic massive
847 sulphide deposits. *Ore Geol. Rev.* **2**, 47-63.

848 Keith M., Haase K. M., Schwarz-Schampera U., Klemd R., Petersen S. and Bach W. (2014) Effects of
849 temperature, sulfur, and oxygen fugacity on the composition of sphalerite from submarine hydrothermal
850 vents. *Geol.* **42**, 699-702.

851 Keith M., Haase K. M., Klemd R., Krumm S. and Strauss H. (2016) Systematic variations of trace element
852 and sulfur isotope compositions in pyrite with stratigraphic depth in the Skouriotissa volcanic-hosted
853 massive sulfide deposit, Troodos ophiolite, Cyprus. *Chem. Geol.* **423**, 7-18.

Kelly D. and Vaughan D. (1983) Pyrrhotine-pentlandite ore textures: a mechanistic approach. *Miner. Mag.* **47**, 453-463.

Kempton P. D., Autio L. K., Rhodes J. M., Holdaway M. J., Dungan M. A. and Johnson P. (1985) Petrology of basalts from hole-504B, deep-sea drilling project, LEG-83. *Initial Reports of the Deep Sea Drilling Project* **83**,129-164.

Kent D. V., Honnorez B., Opdyke N. D. and Fox P. J. (1978) Magnetic properties of dredged oceanic gabbros and the source of marine magnetic anomalies. *Geophy. J. Inter.* **55**, 513-537.

Koepke J., Christie D., Dziony W., Holtz F., Lattard D., Maclennan J., Park S., Scheibner B., Yamasaki T. and Yamazaki S. (2008) Petrography of the dike-gabbro transition at IODP Site 1256 (equatorial Pacific): The evolution of the granoblastic dikes. *Geochem. Geophys. Geosyst.* **9**.

Laverne C., Grauby O., Alt J. C. and Bohn M. (2006) Hydroschorlomite in altered basalts from Hole 1256D, ODP Leg 206: The transition from low-temperature to hydrothermal alteration. *Geochem. Geophys. Geosyst.* **7**.

Lepage L. D. (2003) ILMAT: an Excel worksheet for ilmenite–magnetite geothermometry and geobarometry. *Comp. and Geo.* **29**, 673-678.

Li C. and Ripley E. (2005) Empirical equations to predict the sulfur content of mafic magmas at sulfide saturation and applications to magmatic sulfide deposits. *Miner. Dep.* **40**, 218-230.

MacLean W. H. (1977) Sulfides in Leg 37 drill core from the Mid-Atlantic Ridge. *Can. J. Earth Sci.* **14**, 674-683.

Mathez E.A. (1979) Sulfide relations in Hole 418A flows and sulfur contents of glasses. *Initial Reports of The Deep Sea Drilling Project* **51**, 1069-1085.

875 Metz S. and Trefry J. H. (2000) Chemical and mineralogical influences on concentrations of trace metals
876 in hydrothermal fluids. *Geochim. Cosmochim. Acta* **64**, 2267-2279.

877 Monecke T., Petersen S., Hannington M. D., Grant H. and Samson I. (2016) The minor element
878 endowment of modern sea-floor massive sulfide deposits and comparison with deposits hosted in ancient
879 volcanic successions. *Rev. in Econ. Geol.*

880 Moore J. G. and Calk L. C, (1971) Sulfide spherules in vesicles of dredge pillow basalt. *Am. Miner.*
881 **56**,105-118.

882 Moore J. G. (1975) Mechanism of Formation of Pillow Lava: Pillow lava, produced as fluid lava cools
883 underwater, is the most abundant volcanic rock on earth, but only recently have divers observed it
884 forming. *Am. Sci.* **63**, 269-277.

885 Morse J. and Luther G. (1999) Chemical influences on trace metal-sulfide interactions in anoxic
886 sediments. *Geochim. Cosmochim. Acta* **63**, 3373-3378.

887 Murowchick J. B. and Barnes H. (1986) Marcasite precipitation from hydrothermal solutions. *Geochim.*
888 *Cosmochim. Acta* **50**, 2615-2629.

889 Nadoll P., Angerer T., Mauk J. L., French D. and Walshe J. (2014) The chemistry of hydrothermal
890 magnetite: A review. *Ore Geol. Rev.* **61**, 1-32.

891 Nesbitt B. E., St. Louis R. M. and Muehlenbachs K. (1987) Distribution of gold in altered basalts of
892 DSDP hole 504B. *Can. J. Earth Sci.* **24**, 201-209.

893 Paton C., Hellstrom J., Paul B., Woodhead J. and Hergt J. (2011) Iolite: Freeware for the visualisation and
894 processing of mass spectrometric data. *J. Anal. Atom. Spec.* **26**, 2508-2518.

895 Patten C., Barnes S.-J., Mathez E. A. (2012) Textural variations in MORB sulfide droplets due to
896 differences in crystallization history. *The Can. Miner.* **50**, 675-692

897 Patten C., Barnes S.-J., Mathez E. A. and Jenner F. E. (2013) Partition coefficients of chalcophile
898 elements between sulfide and silicate melts and the early crystallization history of sulfide liquid: LA-ICP-
899 MS analysis of MORB sulfide droplets. *Chem. Geol.* **358**,170-188

900 Patten C. G. C., Pitcairn I. K., Teagle D. A. and Harris M. (2015) Mobility of Au and related elements
901 during the hydrothermal alteration of the oceanic crust: implications for the sources of metals in VMS
902 deposits. *Miner. Dep.*, 1-22.

903 Paton C., Hellstrom J., Paul B., Woodhead J. and Hergt J. (2011) Iolite: Freeware for the visualisation and
904 processing of mass spectrometric data. *J. Anal. Atom. Spec.* **26**, 2508-2518.

905 Richardson C. J., Cann J. R., Richards H. G. and Cowan J. G. (1987) Metal-depleted root zones of the
906 Troodos ore-forming hydrothermal systems, Cyprus. *Earth Planet. Sci. Lett.* **84**, 243-253.

907 Riley J. F. (1977) The pentlandite group (Fe, Ni, Co) 9S8: New data and an appraisal of structure-
908 composition relationships. *Mineral. Mag.* **41**, 345-349.

909 Schiffman P., Bettison L. and Smith B. (1987) Mineralogy and geochemistry of epidosites from the Solea
910 graben, Troodos ophiolite, Cyprus. *Ophiolites: Oceanic Crustal Analogues: Proceedings of the*
911 *Symposium Troodos*, 673-683.

912 Seewald J. S. and Seyfried Jr W. E. (1990) The effect of temperature on metal mobility in subseafloor
913 hydrothermal systems: constraints from basalt alteration experiments. *Earth Planet. Sci. Lett.* **101**, 388-
914 403.

915 Shanks W. C. and Seyfried W. E. (1987) Stable isotope studies of vent fluids and chimney minerals,
916 southern Juan de Fuca Ridge: Sodium metasomatism and seawater sulfate reduction. *J. Geophys. Res.:*
917 *Solid Earth* **92**, 11387-11399.

918 Smedley P. and Kinniburgh D. (2002) A review of the source, behaviour and distribution of arsenic in
919 natural waters. *Applied Geochem.* **17**, 517-568.

920 Stanton R. L. (1972) *Ore petrology*. McGraw-Hill New York.

921 Teagle D., Alt J., Umino S., Miyashita S., Banerjee N. and Wilson D. the Expedition 309/312 Scientists
922 (2006) Superfast spreading rate crust 2 and 3. *Proceedings Integrated Ocean Drilling Program, 309 312*
923 **50**.

924 Tolstoy M., Waldhauser F., Bohnenstiehl D., Weekly R. and Kim W.-Y. (2008) Seismic identification of
925 along-axis hydrothermal flow on the East Pacific Rise. *Nature* **451**, 181-184.

926 Violay M., Pezard P. A., Ildefonse B., Célérier B. and Deleau A. (2012) Structure of the hydrothermal
927 root zone of the sheeted dikes in fast-spread oceanic crust: a core-log integration study of ODP hole
928 1256D, Eastern Equatorial Pacific. *Ofioliti* **37**, 1-11.

929 Wilson DS, et al. (2003). Leg 206 summary. *Proceedings of the Ocean Drilling Programme, Scientific*
930 *Results* **206**

931 Wilson S. A., Ridley W. I. and Koenig A. E. (2002) Development of sulfide calibration standards for the
932 laser ablation inductively-coupled plasma mass spectrometry technique. *J. Anal. Atom. Spec.* **17**, 406-409.

933 Wohlgemuth-Ueberwasser C. C., Ballhaus C., Berndt J., née Paliulionyte V. S. and Meisel T. (2007)
934 Synthesis of PGE sulfide standards for laser ablation inductively coupled plasma mass spectrometry (LA-
935 ICP-MS). *Cont. Miner. Pet.* **154**, 607-617.

936 Wohlgemuth-Ueberwasser C. C., Viljoen F. and McClung C. R. (2014) Metamorphic alteration of the
937 massive sulfide horizon from the Salt River VMS deposit (South Africa). *Ore Geol. Rev.* **56**, 45-52.

938 Wohlgemuth-Ueberwasser C. C., Viljoen F., Petersen S. and Vorster C. (2015) Distribution and solubility
939 limits of trace elements in hydrothermal black smoker sulfides: An in-situ LA-ICP-MS study. *Geochim.*
940 *Cosmochim. Acta* **159**, 16-41.

941 Wolthers M., Van der Linde P. and Van der Weijden C. (1998) Selenium and arsenic in sedimentary
942 pyrites. *Miner. Mag. A* **62**, 1660-1661.

943 Zientek M., Likhachev A., Kunilov V., Barnes S., Meier A., Carlson R., Briggs P., Fries T., Adrian B. and
944 Lightfoot P. (1994) Cumulus processes and the composition of magmatic ore deposits: examples from the
945 Talnakh district, Russia. *Proceedings of the Sudbury-Noril'sk symposium*, 373-392.

946 ## 9. Figure captions

947 Figure 1: Lithostratigraphy at IODP 1256D with Mg# and sulphide proportions in veins. Major
948 secondary minerals and temperature are also shown. Modified from Teagle et al. (2006) and Alt et al.
949 (2010).

950 Figure 2. Sulphide distribution in IODP Hole1256D. The scale corresponds to sulphide proportions with
951 1=trace, 2=discrete, 3=common and 4=major. Yellow boxes are samples with sulphides analysed by
952 EPMA and LA-ICP-MS. Meta. stands for metasomatised sulphides, high T. stands for high temperature
953 sulphides and low T. stands for low temperature sulphides.

954 Figure 3. Reflected light photomicrographs of the magmatic and metasomatised sulphides. Magmatic
955 sulphides: A) Sulphide blebs preserved in the volcanic section composed of pyrrhotite (Po) and
956 chalcopyrite (Cpy). The Po represents the MSS and the Cpy the ISS, see discussion for details. B) Base
957 metal sulphides pyrrhotite-chalcopyrite-pentlandite (Pn) from the plutonic section. Pentlandite is present
958 as lamellae exsolution within the Po which is specific of MSS. Metasomatised sulphides: C) Spherical
959 blebs composed of Py and magnetite (Mag). D) and E) Assemblage from the plutonic section composed of
960 Py-Cpy-Mag; note that the Mag preferentially form a rim. F) Assemblage of Py-Cpy and millerite (Mi)
961 from the plutonic section.

962 Figure 4. Variation of the Ni content versus the Se/As of the pyrites from the different sulphide groups.
963 Metasomatised pyrites are characterised by high Se/As and high Ni, high temperature pyrites by variable
964 Se/As and low Ni and low temperature and patchy pyrites by low Se/As and high Ni. See text for details.

965 Figure 5. Reflected light photomicrographs of the high temperature, low temperature and patchy
966 sulphides. High temperature sulphides: A) pyrite (Py) aggregate in quartz-chlorite vein from the upper
967 sheeted dyke section. The core is formed of small Py grains whereas the rim is formed by large euhedral
968 grains. Presence of chalcopyrite (Cpy) and sphalerite (Sp) with the Cpy disease. B) Large euhedral Py
969 grains in the transitional zone. C) Py and Sp from the mineralised breccia in the transitional zone. Low
970 temperature sulphides: D) Pyrite front in border of an alteration halo. E) Details of the pyrite front with Py
971 and marcasite (Mrc) filling a crack. F) Euhedral Py filling a vesicle. G) Py and trace Cpy in saponite
972 dominated vein. Patchy sulphides: H) and I) Pyrite replacing the silicate matrix and partly the silicate
973 minerals resulting in a patchy aspect.

974 Figure 6. Reflected light photomicrographs of the oxide population in Hole 1256D. A) Skeletal
975 titanomagnetite (T-Mag) in the volcanic section (group 1). M.S.= metasomatised sulphides B) Coarse
976 grain magmatic oxide composed of magnetite (Mag) with ilmenite (Ilm) exsolution (group 2); note the
977 trellis pattern and grain texture. Po=pyrrhotite; Cpy=chalcopyrite. C) Hydrothermal related oxide
978 corresponding to magnetite replacing a silicate phase (group 3). D) Hydrothermal related oxide
979 corresponding to magnetite replacing a sulphide phase (group 3); see discussion. Py=pyrite.

980 Figure 7. Schematic diagram illustrating the paragenesis of the sulphide population at IODP Hole
981 1256D. 1) Magmatic sulphides forming spherical sulphide droplets in the volcanic section and large
982 sulphide aggregates in the plutonic complex. 2) Metasomatised sulphides showing different degrees of
983 sulphide leaching from a) pristine to b) extensively leached. 3) High temperature hydrothermal sulphides
984 precipitated from rising hydrothermal fluids in a) the upper sheeted dykes and b) the mineralised breccia
985 at 1028 mbsf. 4) Low temperature sulphides occurring a) in background altered samples due to low

temperature fluid circulation and b) on borders of alteration halos forming pyrite fronts. 5) Patchy sulphides formed from deep low temperature fluid circulation in the lower part of Hole 1256D. Po=pyrrhotite, Pn=pentlandite, Cpy= chalcopyrite, Py=pyrite, Mag= magnetite, Mi=millerite.

Figure 8. Oxide minerals trace elements. A) Ternary FeO_2, Fe_2O_3 and TiO_2 diagram. Mag=magnetite, Ilm=ilmenite. B) Content of Si and Ca in oxide minerals versus depth. Silica and Ca contents are used as a proxy for the degree of alteration. C) Discrimination diagram for magmatic or hydrothermal origin of magnetite and titanomagnetite with TiO_2<20 wt.%; modified from Dare et al. (2014). Note that skeletal titanomagnetite and coarse magnetite plot in the magmatic field whereas hydrothermal magnetite plots in the hydrothermal field. D) Discrimination diagram showing and titanomagnetite with TiO_2<20 wt.% estimated formation temperature; modified from Nadoll et al. (2014). E) to H) Trace metal content in oxide minerals versus the degree of alteration. See text for details.

Figure 9. Reflected light photomicrographs of metasomatised sulphides showing different degree of sulphide leaching. A) Shadow of magmatic sulphide blebs in the volcanic section with a magnetite (Mag) rim and residual chalcopyrite (Cpy) inside. B) Porous pyrite (Py) surrounded by Mag and trace Cpy in the surroundings. C) and D) Trace leached sulphides with the Mag remaining. B), C) and D) are from the plutonic complex.

Figure 10. Sulphide evolution and metal content variation during metasomatism and leaching. A) Magmatic assemblage characterised by monosulphide solution (MSS) and intermediate solid solution (ISS). During subsolidus reaction MSS exsolve to pyrrhotite (Po) and pentlandite (Pn), and ISS exsolve to chalcopyrite (Cpy). M*=trace metals hosted in Cpy, their behaviour during sulphide evolution is not determined in this study. B) Metal diffusion during metasomatism. Py=pyrite, Mag=magnetite, Mi=millerite. C) and D) Metal mobilisation during partial and extensive sulphide leaching respectively. See text for details.

Figure 11. Trace metal variations in pyrrhotite and metasomatised pyrite during metasomatism and leaching. Selenium is used as proxy to highlight trace metal behaviours both during metasomatism and leaching. Increase concentrations of Se, Te, As, Ag, Au and Zn in metasomatised pyrites are due to residual enrichment by progressive sulphide volume loss first during metasomatism and second by sulphide leaching. See text for details.

Figure 12. Pie charts illustrating the semi-quantitative results of the mass balance calculations. Charts show the proportion to which metals are hosted by different sulfides in %. Magmatic sulphide assemblage is shown as a combination of monosulphide solid solution (MSS) and intermediate solid solution (ISS) because of the too few data available for each sulphide phases in this group. Mass balance calculation cannot be determined for Te and Au in the low temperature sulphides and for Sb in the magmatic sulphides. See Appendix A.4 and B for mass balance calculation results and uncertainties.

Figure 13. Mass variations in the sheeted dyke and plutonic complexes and the associated sulphide population. Mass variations are from whole rock data (Patten et al., 2015). The main sulphide group observed in thin section is shown. No thin sections are available for several samples. Samples hosting metasomatised sulphides show significant metal depletion. See text for details. SD = sheeted dyke complex; PC = plutonic complex.

Table 1. Major and trace metals composition of magmatic sulphides

			S	Fe	Co	Ni	Cu	Zn	As	Se	Ag	Pd	Sb	Te	Ir	Pt	Au	Hg	Pb
			wt.%	wt.%	wt.%	wt.%	wt.%	ppm	ppm	ppm	ppm	ppm	ppm	ppm	ppm	ppm	ppm	ppm	ppm
			EPMA	EPMA	EPMA	LA-ICP-MS	LA-ICP-MS	LA-ICP-MS	LA-ICP-MS	LA-ICP-MS	LA-ICP-MS	LA-ICP-MS	LA-ICP-MS	LA-ICP-MS	LA-ICP-MS	LA-ICP-MS	LA-ICP-MS	LA-ICP-MS	LA-ICP-MS
Po-Cpy intergrowth	mean		39.24	58.0	0.07	0.21	0.58	1054	5.12	56.00	3.44	<D.L.	0.24	2.23	<D.L.	<D.L.	0.066	<D.L.	409.5
EPMA n=11	s.d.		0.7	1.9	0.02	0.02	0.47	987	1.34	15.49	0.93		0.12	0.26			0.049		680.6
LA-ICP-MS n=8	median		39.55	59.0	0.08	0.21	0.69	855	4.90	54.50	3.51		0.24	2.20			0.066		35.1
	range	min	37.6	55.3	0.03	0.18	7.9E-03	47	3.90	36.00	2.12		0.09	2.00			0.031		8.1
		max	39.9	59.6	0.10	0.24	1.28	2900	8.00	89.00	4.80		0.41	2.50			0.100		2100.0
			EPMA	EPMA	EPMA	LA-ICP-MS	LA-ICP-MS	LA-ICP-MS	LA-ICP-MS	LA-ICP-MS	LA-ICP-MS	LA-ICP-MS	LA-ICP-MS	LA-ICP-MS	LA-ICP-MS	LA-ICP-MS	LA-ICP-MS	LA-ICP-MS	LA-ICP-MS
Pyrrhotite	mean		39.57	58.4	0.14	2.18	0.02	9.9	0.95	45.52	0.21	<D.L.	<D.L.	1.25	<D.L.	<D.L.	0.023	<D.L.	0.49
EPMA n=17	s.d.		0.3	0.8	0.27	1.49	0.04	18.1	0.11	8.38	0.11			0.34			0.019		0.22
LA-ICP-MS n=18	median		39.60	58.7	0.07	1.67	1.5E-03	3.8	0.95	44.60	0.17			1.20			0.019		0.57
	range	min	38.5	56.0	0.03	1.15	1.9E-04	1.9	0.87	32.80	0.10			0.67			0.005		0.10
		max	40.0	59.2	1.20	7.50	0.14	78.0	1.02	58.80	0.42			1.81			0.053		0.82
			EPMA	EPMA	EPMA	LA-ICP-MS	EPMA	LA-ICP-MS	LA-ICP-MS	LA-ICP-MS	LA-ICP-MS	LA-ICP-MS	LA-ICP-MS	LA-ICP-MS	LA-ICP-MS	LA-ICP-MS	LA-ICP-MS	LA-ICP-MS	LA-ICP-MS
Chalcopyrite	mean		35.0	31.7	0.28	0.80	31.6	1169	<D.L.	49.64	5.98	<D.L.	<D.L.	2.82	<D.L.	<D.L.	0.027	<D.L.	3.29
EPMA n=14	s.d.		0.2	2.0	0.04	0.99	3.8	1748		18.71	3.38			1.36			0.017		3.64
LA-ICP-MS n=9	median		35.1	30.9	0.30	0.68	33.4	160		46.80	6.76			2.80			0.025		1.30
	range	min	34.6	29.8	0.24	0.01	23.0	2.4		31.50	0.37			0.85			0.012		0.28
		max	35.3	36.8	0.30	3.03	33.7	5000		89.00	10.20			4.40			0.045		10.60
			EPMA	EPMA	EPMA	EPMA													
Pentlandite	mean		42.0	19.8	16.5	21.5	<D.L.	<D.L.	N.D.	N.D.	N.D.	N.D.	N.D.	N.D.	N.D.	N.D.	N.D.	N.D.	N.D.
(n=6)	s.d.		0.4	6.4	3.9	4.0													
	range	min	41.5	11.9	9.5	16.1													
		max	42.3	27.6	21.0	28.5													

The range of composition is reported in the text if the standard deviation is higher than the average; po=pyrrhotite; cpy=chalcopyrite;. s.d.=standard deviation; D.L.=detection limit; N.D.= not determined

Table 2. Major and trace metals composition of metasomatised sulphides

			S	Fe	Co	Ni	Cu	Zn	As	Se	Ag	Pd	Sb	Te	Ir	Pt	Au	Hg	Pb
			wt.%	wt.%	wt.%	wt.%	wt.%	ppm	ppm	ppm	ppm	ppm	ppm	ppm	ppm	ppm	ppm	ppm	ppm
			EPMA	EPMA	EPMA	LA-ICP-MS	LA-ICP-MS	LA-ICP-MS	LA-ICP-MS	LA-ICP-MS	LA-ICP-MS	LA-ICP-MS	LA-ICP-MS	LA-ICP-MS	LA-ICP-MS	LA-ICP-MS	LA-ICP-MS	LA-ICP-MS	LA-ICP-MS
Pyrite	mean		53.0	45.8	0.60	0.51	0.16	76	6.58	108	2.34	4.39	0.77	4.87	<D.L.	1.65	0.07	3.60	16.99
EPMA n=58	s.d.		0.9	1.3	1.32	0.67	0.25	299	9.67	79	5.35	8.48	1.75	8.52		1.62	0.09	2.05	19.38
LA-ICP-MS n=82	median		53.3	46.2	0.08	0.17	0.04	17	3.45	86	0.97	1.16	0.25	2.27		1.16	0.04	3.10	8.93
	range	min	50.2	40.5	0.01	1.8E-03	3.5E-04	1.2	0.42	4	0.08	0.21	0.03	0.50		0.28	0.002	1.40	1.60
		max	54.4	46.9	6.00	2.50	0.91	1870	48.40	470	38.00	25.00	11.80	51.00		4.00	0.31	6.70	94.00
			EPMA	EPMA	EPMA	LA-ICP-MS	EPMA	LA-ICP-MS	LA-ICP-MS	LA-ICP-MS	LA-ICP-MS	LA-ICP-MS	LA-ICP-MS	LA-ICP-MS	LA-ICP-MS	LA-ICP-MS	LA-ICP-MS	LA-ICP-MS	LA-ICP-MS
Chalcopyrite	mean		35.5	31.2	0.106	0.75	32.1	79.1	3.35	76	9.78	<D.L.	0.55	3.55	<D.L.	<D.L.	0.13	11.80	11.48
EPMA n=35	s.d.		2.4	1.9	0.084	1.25	3.6	138	3.64	36	7.37		1.00	3.72			0.18	5.84	8.27
LA-ICP-MS n=20	median		35.1	30.7	0.063	0.14	33.2	27	1.86	72	7.40		0.15	2.03			0.07	12.20	9.85
	range	min	34.5	29.6	0.019	3.5E-03	14.2	7.3	0.42	12	1.46		0.02	0.93			0.01	6.40	1.10
		max	48.9	40.6	0.280	4.10	34.3	500	14.40	150	29.50		3.71	14.00			0.66	18.00	37.80
			EPMA	EPMA	EPMA	EPMA	EPMA	EPMA	LA-ICP-MS	LA-ICP-MS	LA-ICP-MS	LA-ICP-MS	LA-ICP-MS	LA-ICP-MS	LA-ICP-MS	LA-ICP-MS	LA-ICP-MS	LA-ICP-MS	LA-ICP-MS
Millerite	mean		38.2	4.0	6.4	51.3	<D.L.	<D.L.	N.D.	N.D.	N.D.	N.D.	N.D.	N.D.	N.D.	N.D.	N.D.	N.D.	N.D.
(n=6)	s.d.		3.5	1.9	7.6	12.3													
	range	min	35.2	2.5	0.02	33.4													
		max	42.5	7.6	14.8	61.6													

s.d.=standard deviation; D.L.=detection limit; N.D.= not determined

Table 3. Major and trace metals composition of high temperature sulphides

		S	Fe	Co	Ni	Cu	Zn	As	Se	Ag	Pd	Sb	Te	Ir	Pt	Au	Hg	Pb
		wt.%	wt.%	wt.%	ppm	ppm	ppm	ppm	ppm	ppm	ppm	ppm	ppm	ppm	ppm	ppm	ppm	ppm
		EPMA	EPMA	EPMA	LA-ICP-MS	LA-ICP-MS	LA-ICP-MS	LA-ICP-MS	LA-ICP-MS	LA-ICP-MS	LA-ICP-MS	LA-ICP-MS	LA-ICP-MS	LA-ICP-MS	LA-ICP-MS	LA-ICP-MS	LA-ICP-MS	LA-ICP-MS
All pyrites	mean	53.8	46.6	0.11	124	44.1	46.0	23.94	66.76	2.45	0.17	0.61	1.63	<D.L.	<D.L.	0.12	1.89	69.72
EPMA n=62	s.d.	0.5	0.5	0.09	205	60.8	187.6	19.93	170.07	2.40	0.10	0.78	2.22			0.10	1.76	97.73
LA-ICP-MS n=105	median	53.9	46.8	0.09	30.0	25.9	5.9	23.70	31.50	2.39	0.13	0.33	1.09			0.12	1.24	14.60
	range min	52.3	44.5	0.01	0.95	0.7	0.6	0.67	1.27	0.09	0.10	0.04	0.46			0.02	0.64	0.50
	range max	54.6	47.8	0.32	1225	390.0	1600.0	93.00	1243.00	12.10	0.29	4.07	14.20			0.58	7.60	408.00
Transitional zone pyrite	mean	53.7	46.8	0.10	50	34.7	52.0	31.11	88.50	2.49	0.11	0.67	2.45	<D.L.	<D.L.	0.12	1.71	104.63
EPMA n=28	s.d.	0.5	0.3	0.11	111	28.7	222.9	18.68	231.45	2.18	0.02	0.80	4.14			0.10	1.71	107.52
LA-ICP-MS n=36	median	53.8	46.8	0.05	19.3	29.6	5.7	32.15	34.15	2.57	0.11	0.47	1.17			0.12	1.02	68.80
	range min	52.5	46.3	0.01	0.95	0.7	0.6	0.67	1.27	0.09	0.10	0.04	0.51			0.02	0.64	0.50
	range max	54.4	47.8	0.32	578	136.0	1600.0	93.00	1243.00	9.59	0.13	4.07	14.20			0.58	7.60	408.00
Upper sheeted dyke pyrite	mean	53.9	46.5	0.12	236	60.4	35.0	6.15	42.41	2.38	<D.L.	0.07	1.33	<D.L.	<D.L.	<D.L.	3.45	8.13
EPMA n=34	s.d.	0.5	0.6	0.04	260	91.9	94.6	8.59	35.13	2.81		0.03	0.72				1.91	11.05
LA-ICP-MS n=69	median	53.9	46.7	0.11	174.5	21.3	6.5	3.44	30.80	1.58		0.06	1.09				3.45	4.22
	range min	52.3	44.5	0.06	11.80	0.9	0.9	0.69	12.90	0.12		0.04	0.46				2.10	0.69
	range max	54.6	47.1	0.18	1225	390.0	419.0	41.40	187.00	12.10		0.13	2.88				4.80	52.60
		EPMA	EPMA	EPMA	LA-ICP-MS	EPMA (wt.%)	LA-ICP-MS	LA-ICP-MS	LA-ICP-MS	LA-ICP-MS	LA-ICP-MS	LA-ICP-MS	LA-ICP-MS	LA-ICP-MS	LA-ICP-MS	LA-ICP-MS	LA-ICP-MS	LA-ICP-MS
Chalcopyrite	mean	35.0	30.2	<D.L.	237	33.5	1701	1.73	160.25	5.95	<D.L.	0.31	1.04	<D.L.	<D.L.	<D.L.	<D.L.	11.49
EPMA n=29	s.d.	0.4	0.8		203	0.5	3755	0.89	197.92	4.56		0.28	0.44					8.99
LA-ICP-MS n=12	median	35.1	30.4		197	33.7	714	1.90	67.90	6.20		0.17	1.10					8.97
	range min	34.1	28.5		49.0	32.5	2.2	0.37	11.00	0.37		0.12	0.49					1.53
	range max	35.5	31.3		591	34.0	12900	2.50	566.00	14.50		0.80	1.50					28.70
		EPMA	EPMA	EPMA	LA-ICP-MS	LA-ICP-MS	EPMA (wt.%)	LA-ICP-MS	LA-ICP-MS	LA-ICP-MS	LA-ICP-MS	LA-ICP-MS	LA-ICP-MS	LA-ICP-MS	LA-ICP-MS	LA-ICP-MS	LA-ICP-MS	LA-ICP-MS
Sphalerite	mean	33.7	8.5	0.03	39.1	6683	55.2	12.24	17.42	3.59	<D.L.	22.42	<D.L.	<D.L.	<D.L.	0.02	95.42	65.45
EPMA n=19	s.d.	0.3	3.1	0.01	35.6	12071	2.9	8.38	11.13	3.49		17.47				0.01	113.16	58.45
LA-ICP-MS n=10	median	33.6	9.8	0.03	30.3	1650	54.2	11.50	14.40	1.73		20.90				0.02	55.50	52.55
	range min	33.2	2.1	0.02	6.0	126	51.9	0.57	4.30	1.46		0.06				0.01	10.50	8.49
	range max	34.2	12.3	0.06	110.0	37900	61.3	23.30	29.50	12.00		52.90				0.03	310.00	190.00

s.d.=standard deviation; D.L.=detection limit; N.D.= not determined

Table 4. Major and trace metlas composition of low temperature sulphides

		S	Fe	Co	Ni	Cu	Zn	As	Se	Ag	Pd	Sb	Te	Ir	Pt	Au	Hg	Pb
		wt.%	wt.%	wt.%	wt.%	ppm	ppm	ppm	ppm	ppm	ppm	ppm	ppm	ppm	ppm	ppm	ppm	ppm
		EPMA	EPMA	EPMA	LA-ICP-MS	LA-ICP-MS	LA-ICP-MS	LA-ICP-MS	LA-ICP-MS	LA-ICP-MS	LA-ICP-MS	LA-ICP-MS	LA-ICP-MS	LA-ICP-MS	LA-ICP-MS	LA-ICP-MS	LA-ICP-MS	LA-ICP-MS
Pyrite/Marcasite	mean	52.7	46.3	0.06	0.20	9.6	3.3	102	37	0.20	<D.L.	0.38	<D.L.	<D.L.	<D.L.	<D.L.	<D.L.	1.37
EPMA n=28	s.d.	0.6	0.5	0.08	0.30	11.2	2.8	67	14	0.10		0.24						1.26
LA-ICP-MS n=28	median	52.9	46.5	0.04	0.06	6.0	3.3	98	38	0.17		0.33						0.9
	range min	51.1	45.1	0.01	0.01	1.0	0.7	9.1	18	0.10		0.09						0.12
	range max	53.6	47.0	0.26	1.07	57.0	14	271	61	0.42		1.03						4

s.d.=standard deviation; D.L.=detection limit; N.D.= not determined

Table 5. Major and trace metals composition of patchy sulphides

		S	Fe	Co	Ni	Cu	Zn	As	Se	Ag	Pd	Sb	Te	Ir	Pt	Au	Hg	Pb
		wt.%	wt.%	wt.%	wt.%	wt.%	ppm	ppm	ppm	ppm	ppm	ppm	ppm	ppm	ppm	ppm	ppm	ppm
		EPMA	EPMA	EPMA	LA-ICP-MS	LA-ICP-MS	LA-ICP-MS	LA-ICP-MS	LA-ICP-MS	LA-ICP-MS	LA-ICP-MS	LA-ICP-MS	LA-ICP-MS	LA-ICP-MS	LA-ICP-MS	LA-ICP-MS	LA-ICP-MS	LA-ICP-MS
Pyrite	mean	53.2	46.2	0.28	0.34	0.022	9.34	43.60	34.44	0.60	<D.L.	2.67	3.12	<D.L.	<D.L.	0.028	<D.L.	9.58
EPMA n=31	s.d.	0.9	1.0	0.34	0.61	0.088	18.37	35.32	26.87	0.72		1.62	1.68			0.027		14.80
LA-ICP-MS n=39	median	53.4	46.5	0.15	0.11	0.001	2.22	43.00	28.00	0.28		2.82	3.00			0.015		4.01
	range min	50.4	42.2	0.01	4E-03	8E-05	0.65	0.65	3.10	0.09		0.09	1.50			0.003		0.30
	range max	53.9	47.2	1.26	3.11	0.530	89.00	118.80	104.40	2.54		6.64	4.86			0.081		75.70
		EPMA	EPMA	EPMA	LA-ICP-MS	EPMA	LA-ICP-MS	LA-ICP-MS	LA-ICP-MS	LA-ICP-MS	LA-ICP-MS	LA-ICP-MS	LA-ICP-MS	LA-ICP-MS	LA-ICP-MS	LA-ICP-MS	LA-ICP-MS	LA-ICP-MS
Chalcopyrite	mean	34.8	30.4	0.55	0.14	32.72	1170	<D.L.	<D.L.	2.01	<D.L.	<D.L.	<D.L.	<D.L.	<D.L.	<D.L.	<D.L.	20.75
EPMA n=4	s.d.	0.3	0.9	0.76	0.17	0.98	1556			0.01								16.19
LA-ICP-MS n=2	range min	34.2	29.4	0.01	0.02	31.25	69			2.00								9.30
	range max	34.8	31.6	1.08	0.26	33.28	2270			2.01								32.20

s.d.=standard deviation; D.L.=detection limit; N.D.= not determined

Table 6. Composition of oxide minerals at IODP Hole 1256D; σ= standard deviation

		Magmatic Skeletal Titanomagnetite	Magmatic Ilmenite	Magmatic Magnetite	Hydrothermal Magnetite
			EPMA (wt.%)		
SiO_2	average	**0.49**	**0.12**	**0.17**	**0.59**
	σ	0.41	0.07	0.08	0.65
Al_2O_3	average	**1.62**	**0.07**	**1.13**	**0.63**
	σ	0.47	0.04	0.47	0.36
MgO	average	**0.24**	**0.22**	**0.07**	**0.15**
	σ	0.10	0.16	0.04	0.23
MnO	average	**0.68**	**0.92**	**0.11**	**0.11**
	σ	0.43	0.31	0.06	0.09
TiO_2	average	**17.83**	**48.75**	**3.44**	**1.73**
	σ	6.49	1.45	1.41	1.45
CaO	average	**0.17**	**0.06**	**0.05**	**0.25**
	σ	0.17	0.06	0.04	0.28
FeO	average	**46.5**	**42.6**	**34.3**	**32.3**
	σ	5.70	1.26	0.83	1.18
Fe_2O_3*	average	**29.2**	**6.2**	**57.9**	**61.9**
	σ	12.51	2.53	2.13	3.24
Total	average	**97.4**	**99.4**	**98.9**	**98.1**
	σ	1.87	0.67	0.44	0.88
			LA-ICP-MS (ppm)		
			Magmatic Mixed signal		
51V	average	**4204**	**3959**		**2666**
	σ	1905	2925		610
	median	4505	2710		2580
	min	88	1142		2110
	max	8850	10100		3700
52Cr	average	**16**	**174**		**107**
	σ	27	238		119
	median	8	58		70
	min	2	6		16
	max	139	1008		314
60Ni	average	**101**	**229**		**676**
	σ	73	482		499
	median	84	112		477
	min	24	51		224
	max	310	3390		1420
65Cu	average	**55**	**31**		**44**
	σ	76	64		41
	median	21	9		33
	min	5	2		8
	max	316	277		102
66Zn	average	**1582**	**251**		**118**
	σ	764	195		82
	median	1517	158		86
	min	37	72		68
	max	3120	732		262
121Sb	average	**0.26**	**0.17**		**>d.l.**
	σ	0.23	0.01		
	median	0.14	0.17		
	min	0.12	0.16		
	max	0.72	0.18		
208Pb	average	**2.62**	**2.30**		**1.76**
	σ	4.00	4.65		0.70
	median	1.31	0.43		2.00
	min	0.08	0.11		0.73
	max	19.60	23.50		2.30

σ= standard deviation;Fe_2O_3* is calculated is calculated using Carmichael (1966) and Lepage (2003) method.

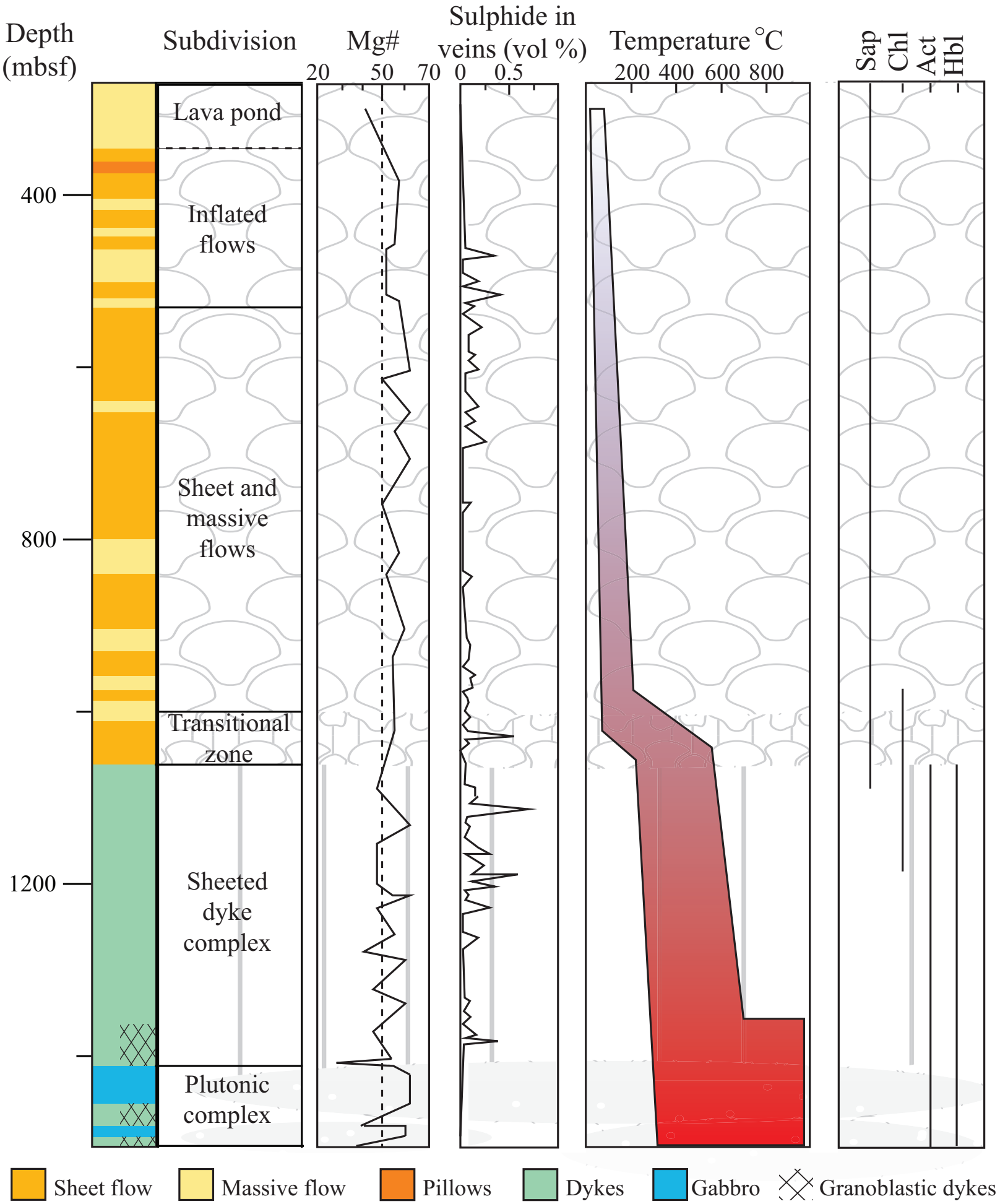
Depth (mbsf)
Subdivision
Mg#
20
50
70
Sulphide in veins (vol %)
0
0.5
Temperature °C
200
400
600
800
Sap
Chl
Act
Hbl
400
800
1200
Lava pond
Inflated flows
Sheet and massive flows
Transitional zone
Sheeted dyke complex
Plutonic complex
Sheet flow
Massive flow
Pillows
Dykes
Gabbro
Granoblastic dykes

Figure 1.

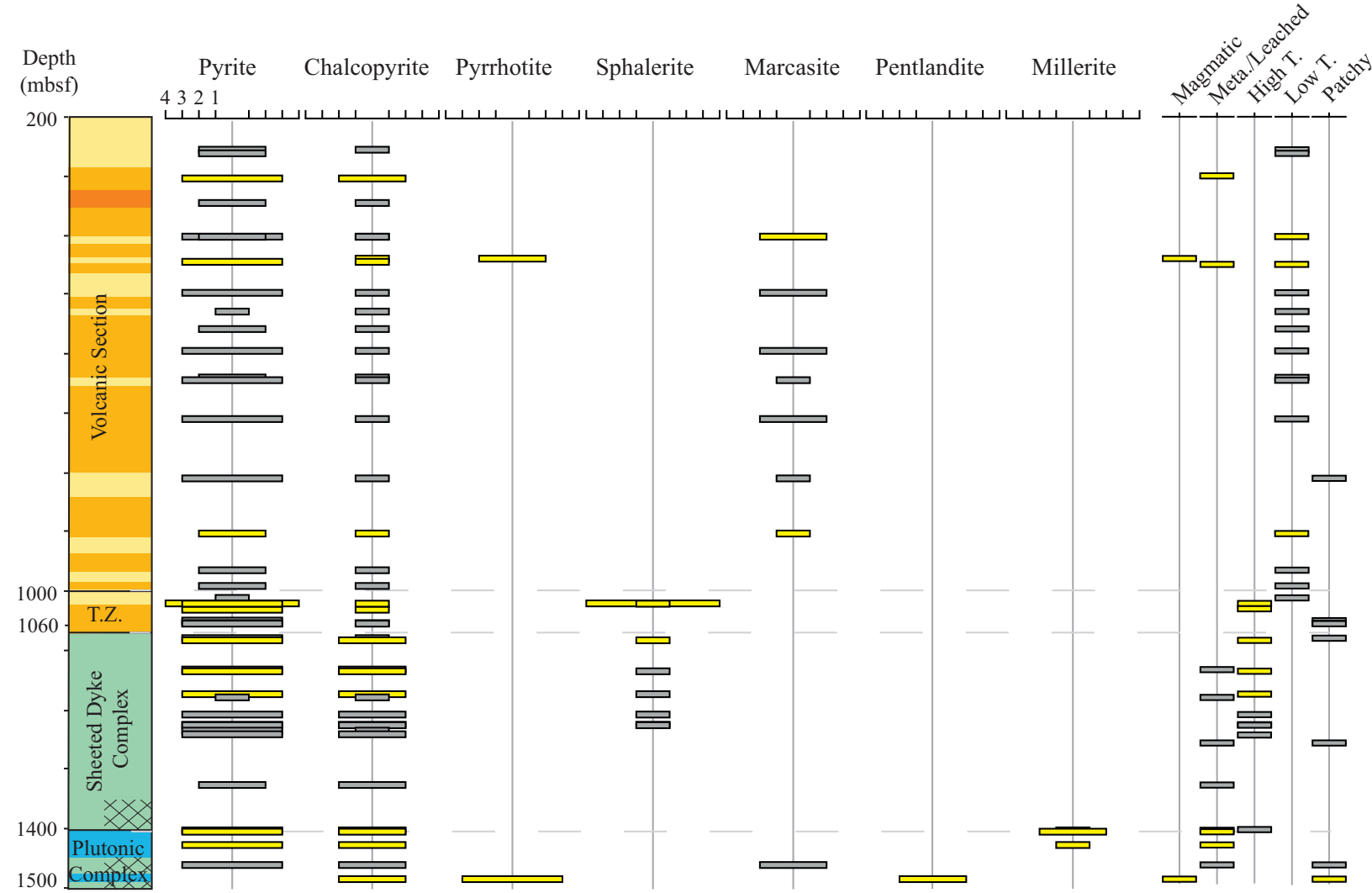
Depth
(mbsf)
Pyrite
Chalcopyrite
Pyrrhotite
Sphalerite
Marcasite
Pentlandite
Millerite
4 3 2 1
Magmatic
Meta./Leached
High T.
Low T.
Patchy
200
1000
1060
1400
1500
Volcanic Section
T.Z.
Sheeted Dyke Complex
Plutonic Complex

Figure 2.

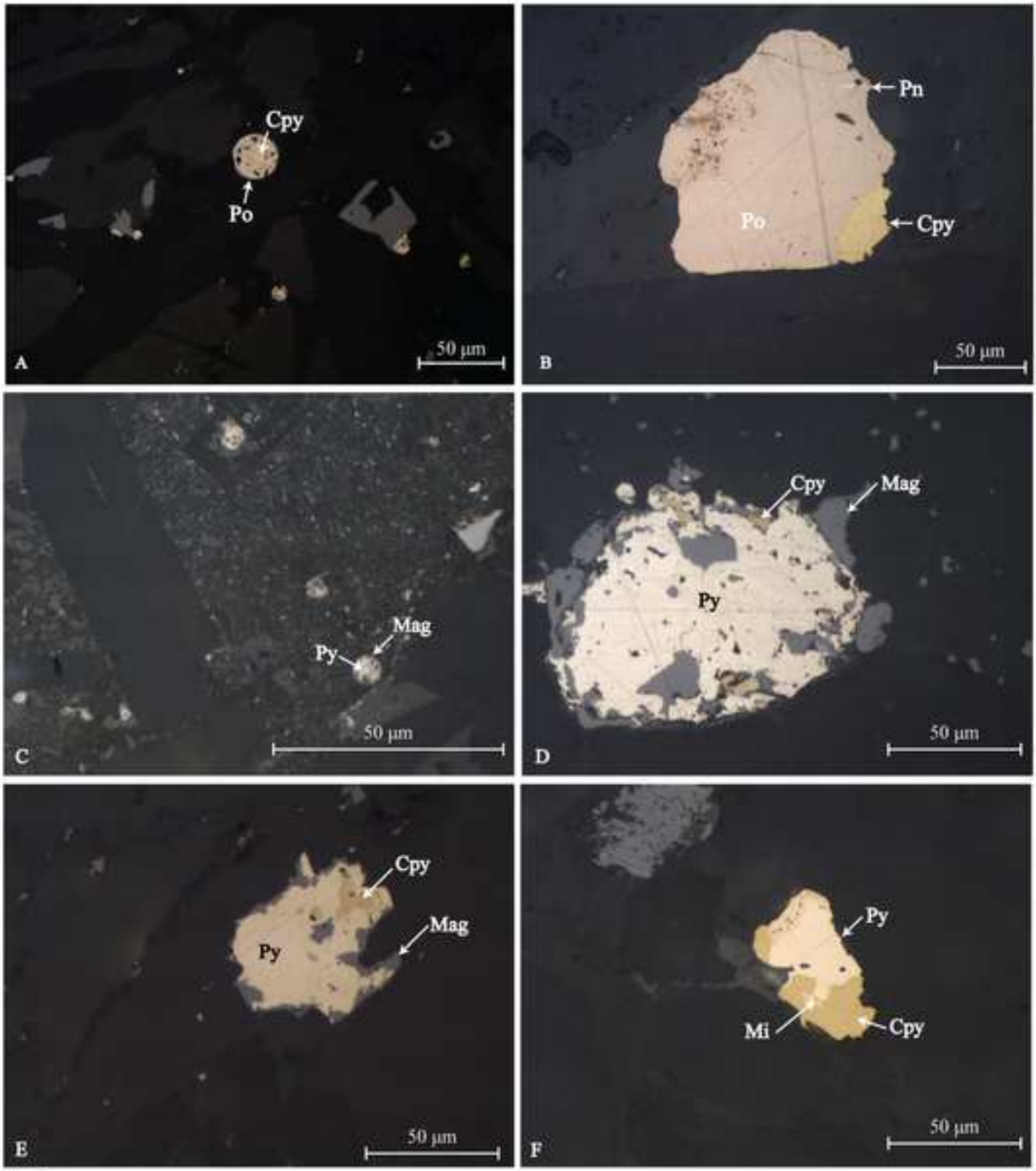
Cpy
Po
50 µm
A
Pn
Po
Cpy
50 µm
B
Mag
Py
50 µm
C
Cpy
Mag
Py
50 µm
D
Cpy
Mag
Py
50 µm
E
Py
Mi
Cpy
50 µm
F

Figure 3.

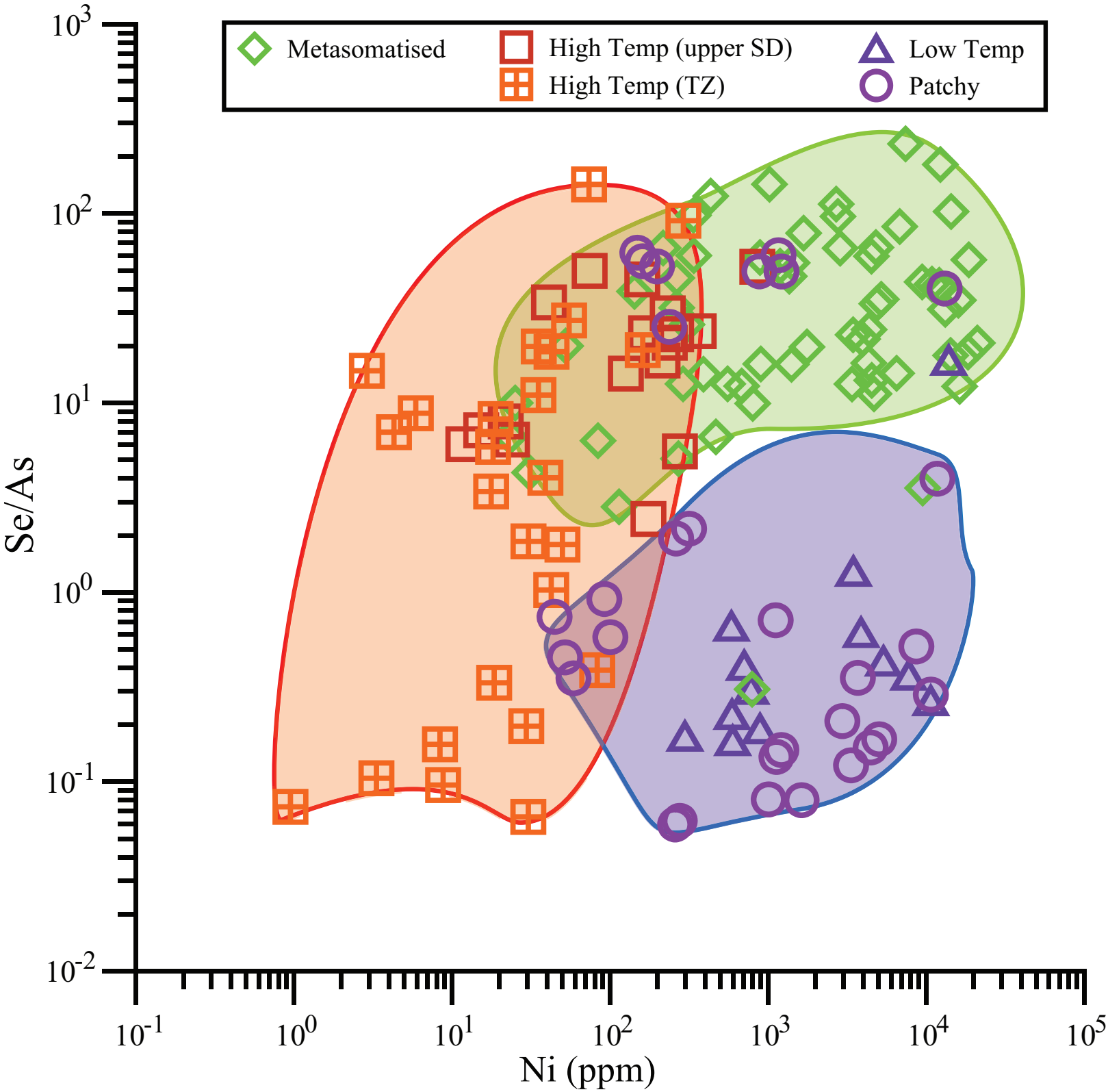
Metasomatised
High Temp (upper SD)
High Temp (TZ)
Low Temp
Patchy
Se/As
Ni (ppm)
10^3
10^2
10^1
10^0
10^-1
10^-2
10^-1
10^0
10^1
10^2
10^3
10^4
10^5

Figure 4.

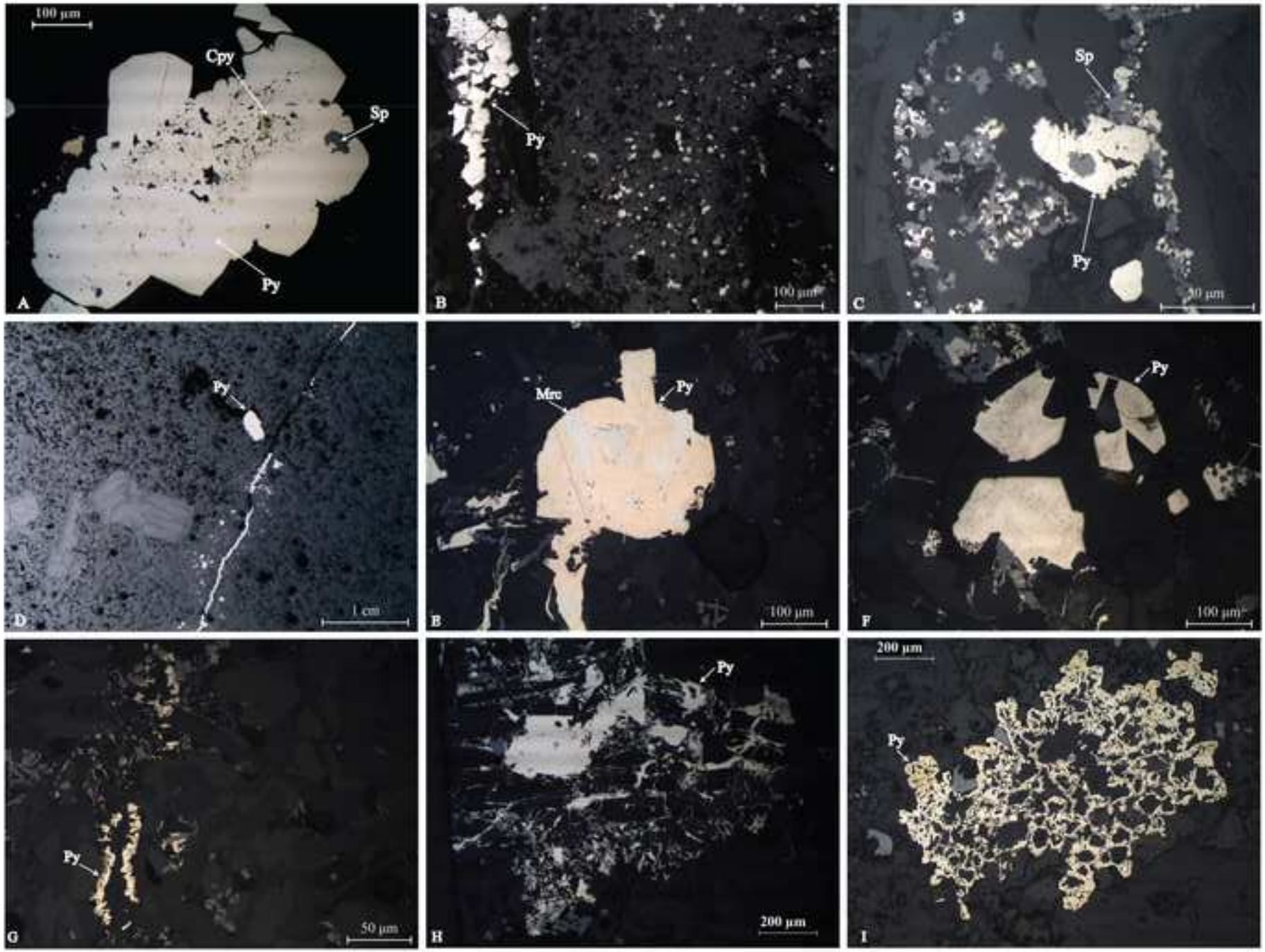
100 µm
Cpy
Sp
Py
A
Py
100 µm
B
Sp
Py
20 µm
C
Py
1 cm
D
Mrc
Py
100 µm
E
Py
100 µm
F
Py
50 µm
G
Py
200 µm
H
200 µm
Py
I

Figure 5.

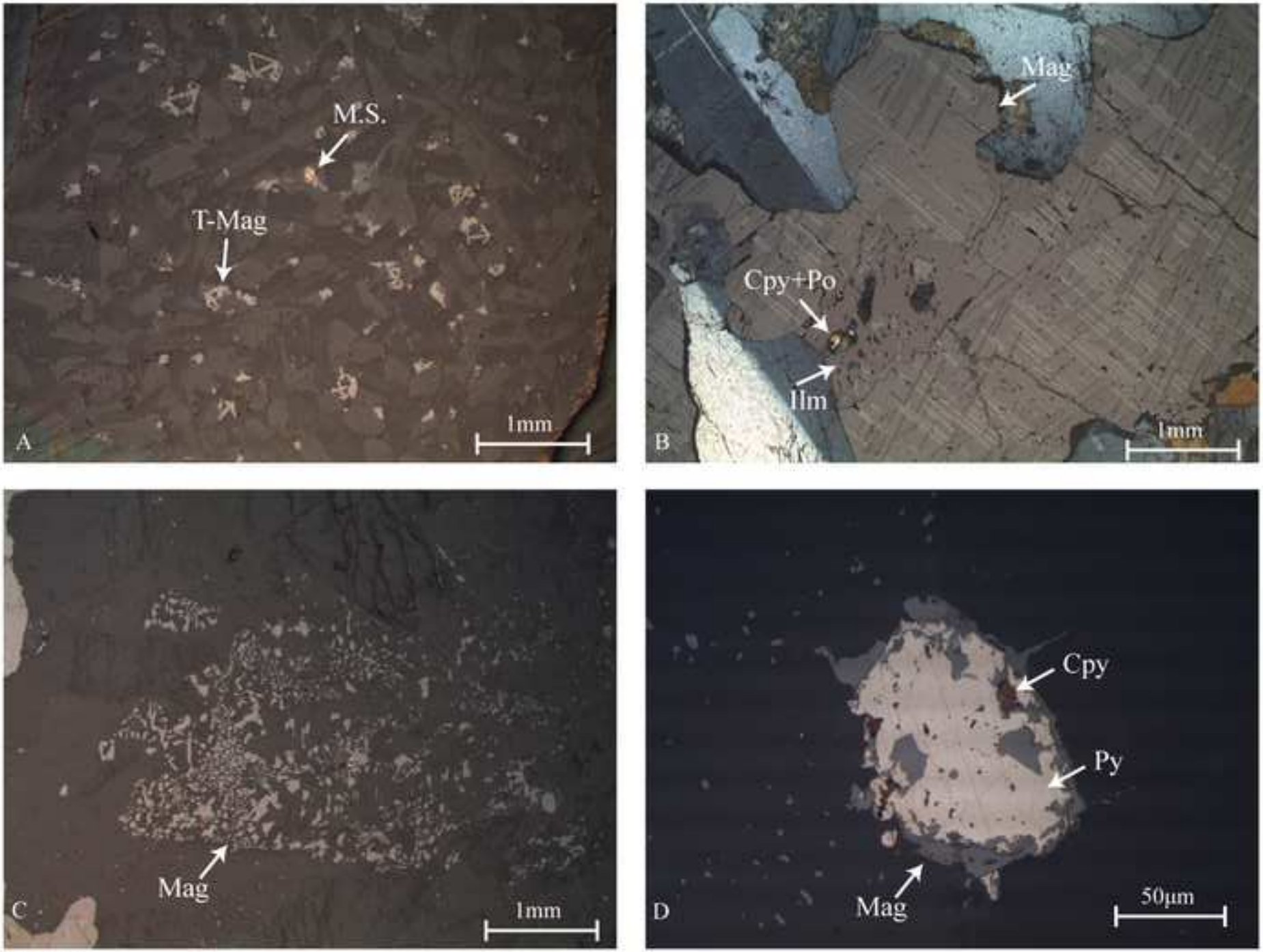

Figure 6.

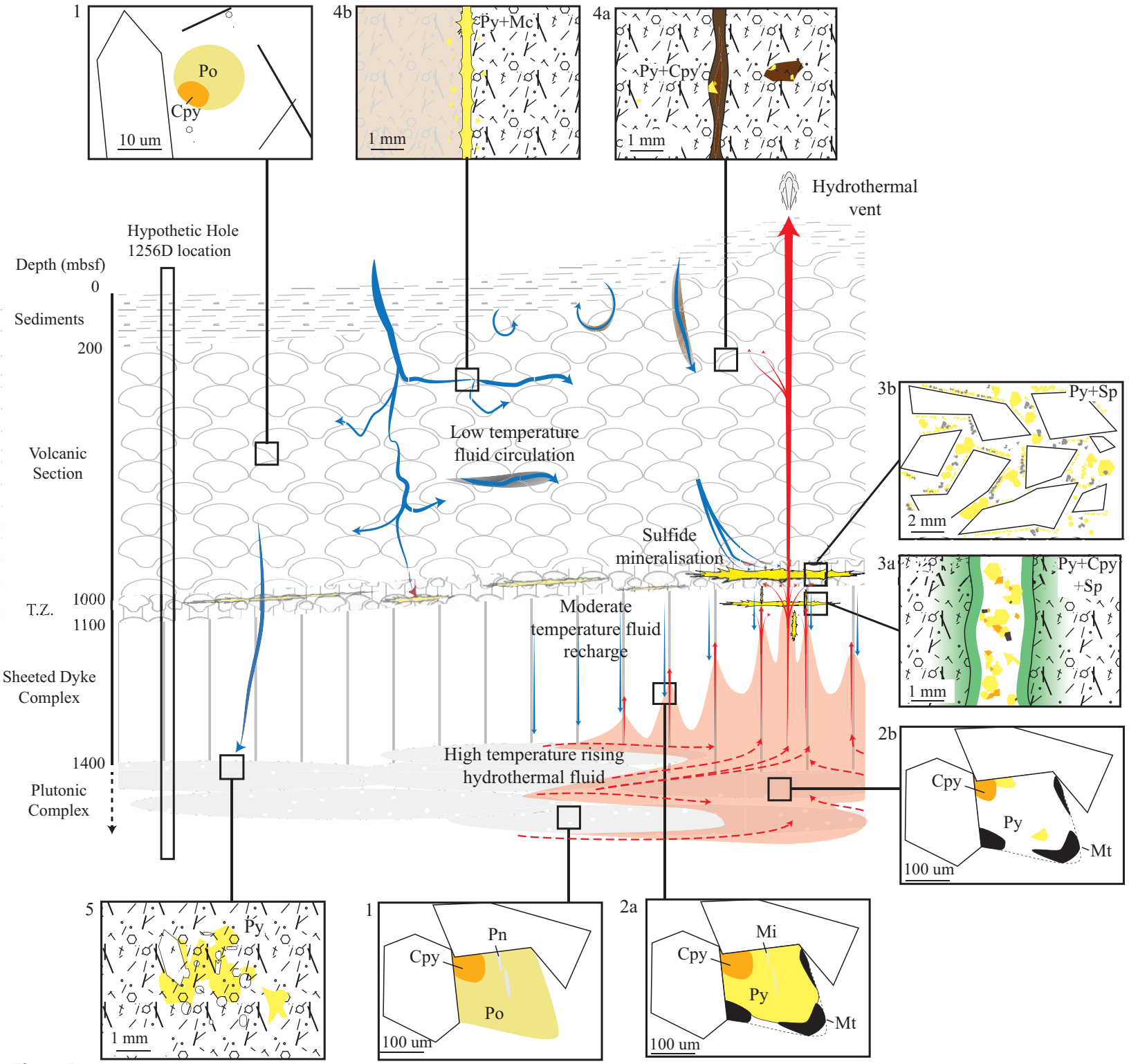
1
Po
Cpy
10 um
4b
Py+Mc
1 mm
4a
Py+Cpy
1 mm
Hydrothermal vent
Hypothetic Hole 1256D location
Depth (mbsf)
0
Sediments
200
Volcanic Section
Low temperature fluid circulation
Sulfide mineralisation
3b
Py+Sp
2 mm
3a
Py+Cpy +Sp
1 mm
T.Z.
1000
1100
Moderate temperature fluid recharge
Sheeted Dyke Complex
1400
Plutonic Complex
High temperature rising hydrothermal fluid
2b
Cpy
Py
Mt
100 um
5
Py
1 mm
1
Pn
Cpy
Po
100 um
2a
Mi
Cpy
Py
Mt
100 um

Figure 7.

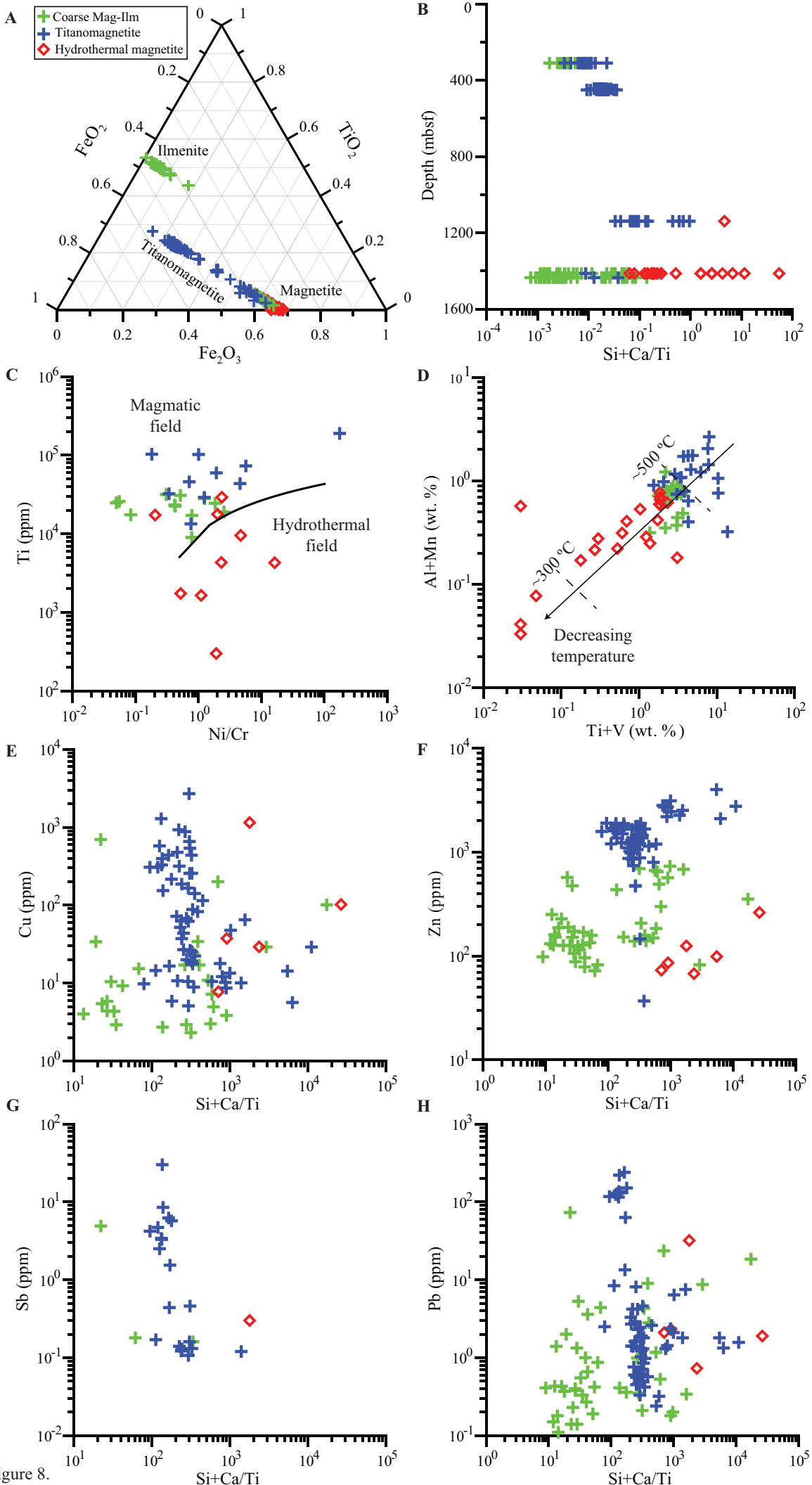
A
Coarse Mag-Ilm
Titanomagnetite
Hydrothermal magnetite
FeO
TiO
Ilmenite
Titanomagnetite
Magnetite
Fe2O3
B
Depth (mbsf)
Si+Ca/Ti
C
Magmatic field
Hydrothermal field
Ti (ppm)
Ni/Cr
D
~500 °C
~300 °C
Decreasing temperature
Al+Mn (wt. %)
Ti+V (wt. %)
E
Cu (ppm)
Si+Ca/Ti
F
Zn (ppm)
Si+Ca/Ti
G
Sb (ppm)
Si+Ca/Ti
H
Pb (ppm)
Si+Ca/Ti

Figure 8.

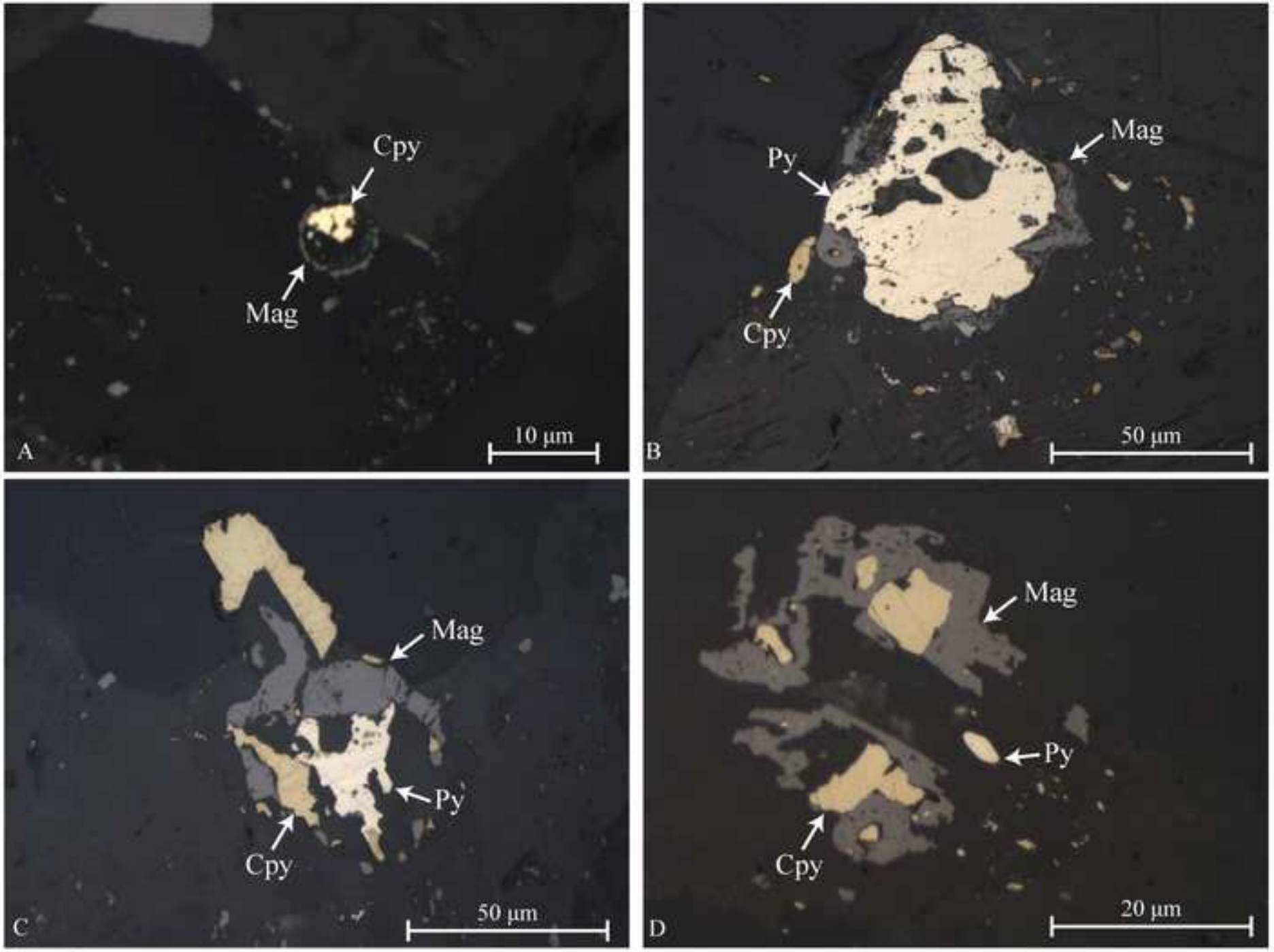
Cpy
Mag
10 µm
A
Py
Mag
Cpy
50 µm
B
Mag
Py
Cpy
50 µm
C
Mag
Py
Cpy
20 µm
D

Figure 9.

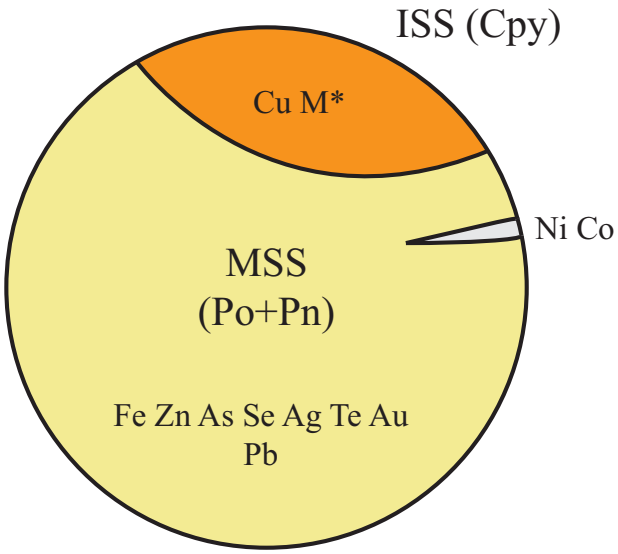

A. Magmatic assemblage
High temperature 1200-650ºC

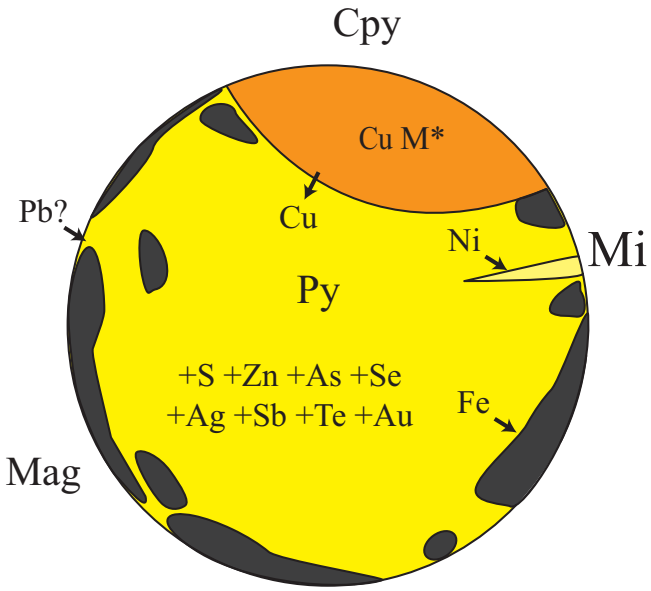

B. Metasomatism
Oxidation by moderate temperature hydrothermal fluids (250-350ºC)

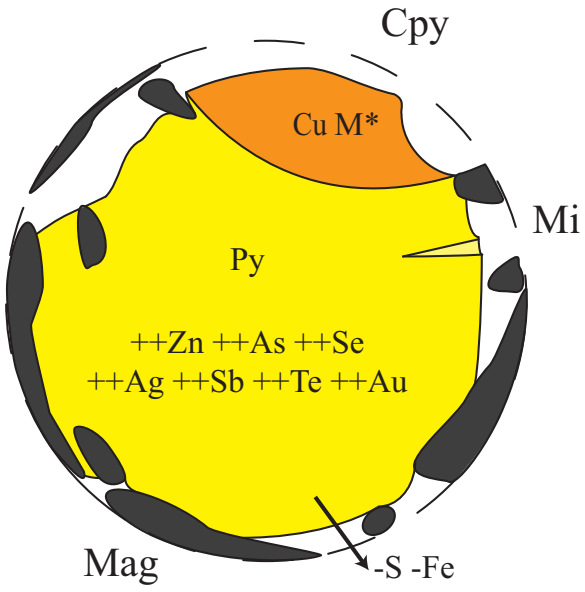

C. Partial sulphide leaching
Leaching by high temperature hydrothermal fluids (>350ºC)

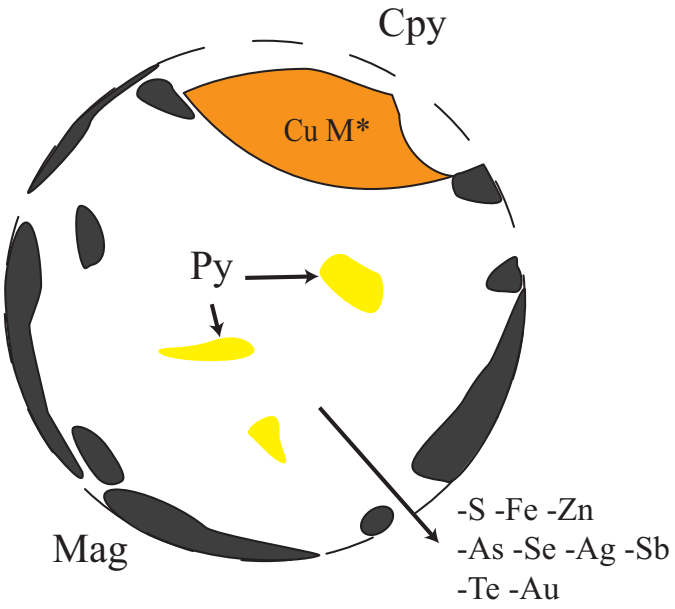

D. Extensive sulphide leaching
Leaching by high temperature hydrothermal fluids (>350ºC)

Figure 10.

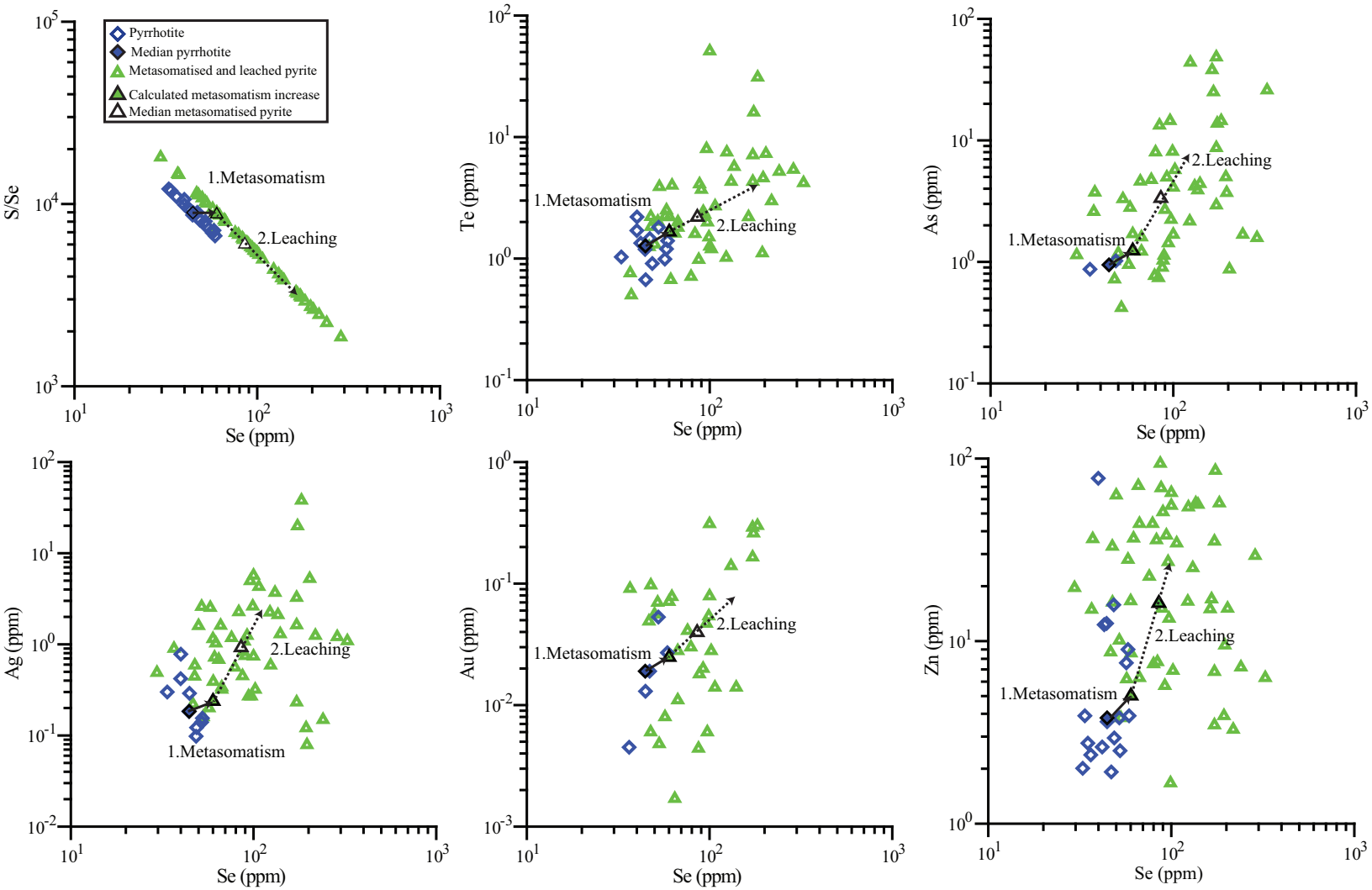
Pyrrhotite
Median pyrrhotite
Metasomatised and leached pyrite
Calculated metasomatism increase
Median metasomatised pyrite
S/Se
Se (ppm)
1.Metasomatism
2.Leaching
Te (ppm)
As (ppm)
Ag (ppm)
Au (ppm)
Zn (ppm)

Figure. 11

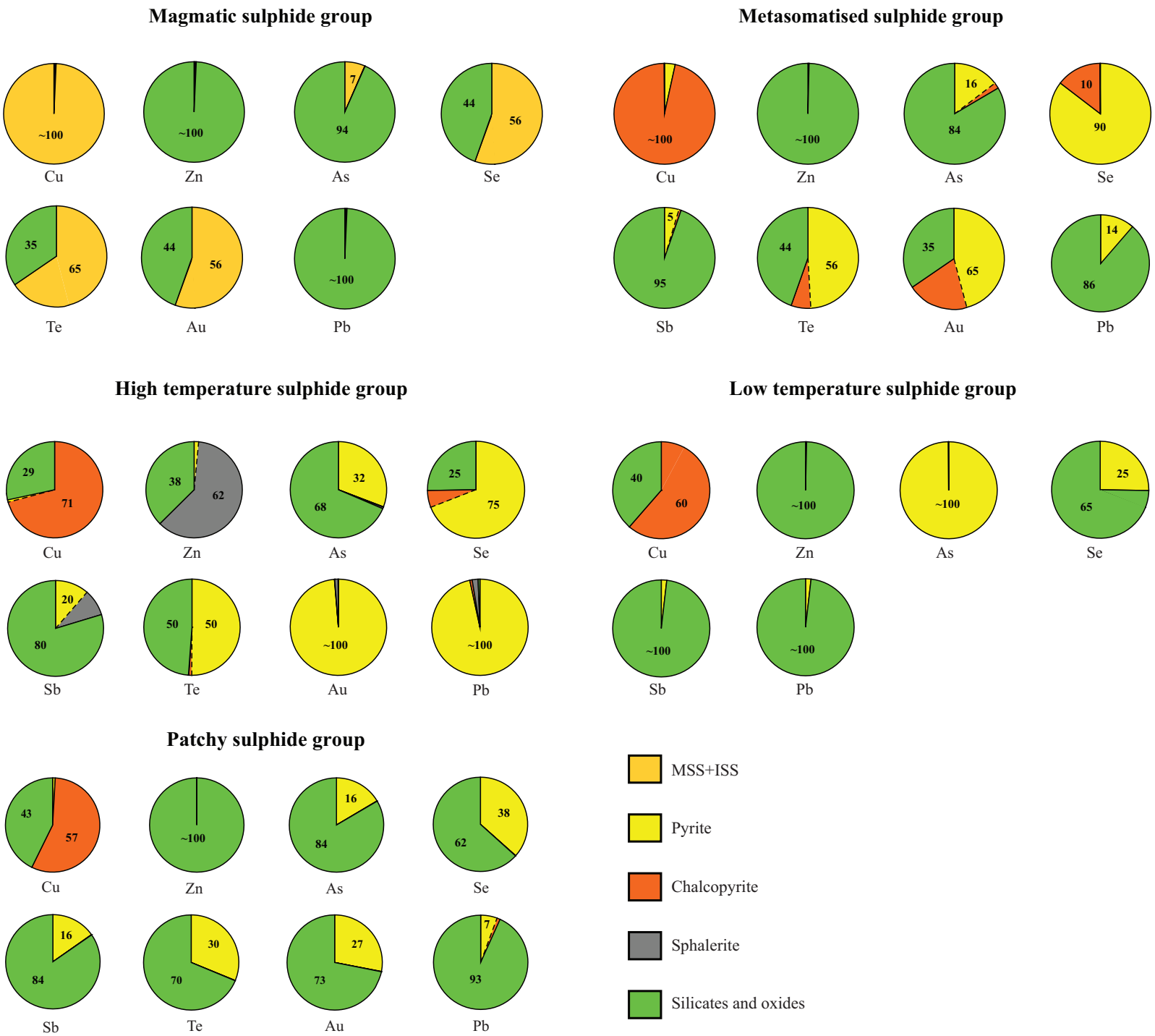
Magmatic sulphide group
~100
Cu
~100
Zn
7
94
As
44
56
Se
35
65
Te
44
56
Au
~100
Pb
Metasomatised sulphide group
~100
Cu
~100
Zn
16
84
As
10
90
Se
5
95
Sb
44
56
Te
35
65
Au
14
86
Pb
High temperature sulphide group
29
71
Cu
38
62
Zn
32
68
As
25
75
Se
20
80
Sb
50
50
Te
~100
Au
~100
Pb
Low temperature sulphide group
40
60
Cu
~100
Zn
~100
As
25
65
Se
~100
Sb
~100
Pb
Patchy sulphide group
43
57
Cu
~100
Zn
16
84
As
38
62
Se
16
84
Sb
30
70
Te
27
73
Au
7
93
Pb
MSS+ISS
Pyrite
Chalcopyrite
Sphalerite
Silicates and oxides

Figure 12.

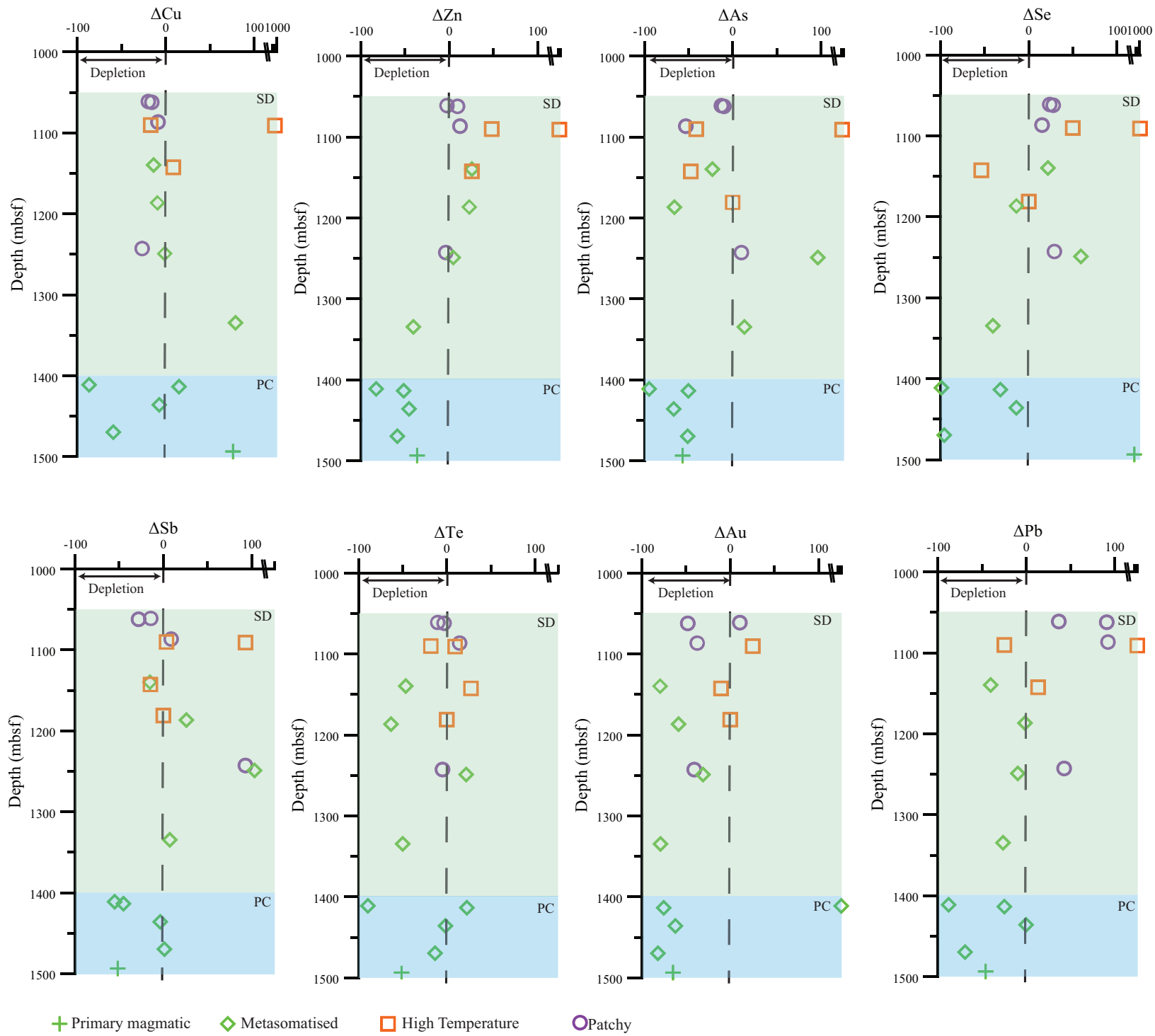
ΔCu
ΔZn
ΔAs
ΔSe
ΔSb
ΔTe
ΔAu
ΔPb
Depletion
SD
PC
Depth (mbsf)
Primary magmatic
Metasomatised
High Temperature
Patchy

Figure 13.